OPEN

NPG Asia Materials (2016) 8, e320; doi:10.1038/am.2016.154
www.nature.com/am

ORIGINAL ARTICLE

Crystal metamorphosis at stress extremes: how soft phonons turn into lattice defects

Xiaohui Liu[1,2], Jianfeng Gu[1], Yao Shen[1] and Ju Li[2,3]

At 0 K, phonon instability controls the ideal strength and the ultrafast dynamics of defect nucleation in perfect crystals under high stress. However, how a soft phonon evolves into a lattice defect is still unclear. Here, we develop a full-Brillouin zone soft-phonon-searching algorithm that shows outstanding accuracy and efficiency for pinpointing general phonon instability within the joint material-reciprocal (x–k) spaces. By combining finite-element modeling with embedded phonon algorithm and atomistic simulation, we show how a zone-boundary soft phonon is first triggered in a simple metal (aluminum) under nanoindentation, subsequently leading to a transient new crystal phase and ensuing nucleation of a deformation twin with only one-half of the transformation strain of the conventional twin. We propose a two-stage mechanism governing the transformation of unstable short-wave phonons into lattice defects, which is fundamentally different from that initially triggered by soft long-wavelength phonons. The uncovered material dynamics at stress extremes reveal deep connections between delocalized phonons and localized defects trapped by the full nonlinear potential energy landscape and add to the rich repertoire of nonlinear dynamics found in nature.
NPG Asia Materials (2016) **8,** e320; doi:10.1038/am.2016.154; published online 21 October 2016

INTRODUCTION

The strength of solids at temperature $T=0$ K limits the attainable range of elastic strain engineering,[1] whereby finite elastic strain field[2,3] $\boldsymbol{\varepsilon}(\mathbf{x})$ is tuned to yield better transistors,[1] solar cells,[2] superconductors[4] and other devices. Phonon instability[5] controls the ideal strength[6] and influences stress-driven defect nucleation and/or phase transformation in an initially perfect crystalline lattice at 0 K. When a phonon frequency ω becomes imaginary, the harmonic oscillation will grow in amplitude and subsequently break lattice translational symmetry leading to defect nucleation.[7,8]

Such processes are believed to occur in some low-temperature nanoindentation experiments where near-ideal strengths are experimentally measured.[6] Previous simulation studies have focused on the long-wave phonon instability (elastic instability) with wave vector $\mathbf{k}\approx 0$ (Γ point) in the Brillouin zone (BZ) where an analytical formula can be derived based on the elastic constants and stress.[7–12] However, the long-wave instability is just one special class of the general phonon instability in full BZ,[13–23] which may be diagnosed by phonon calculation for homogeneously strained crystals under periodical boundary conditions (PBCs).[5] While for crystals with inhomogeneous strain during nanoindentation, where BZ and PBC become ill-defined as a result of losing the lattice translational symmetry, it is reasonable to turn to examine the structural stability of each infinite lattice Θ that is homogeneously strained according to the local deformation at each material point $\mathbf{x}$, if the material strain field is slowly varied. This is because the incipient instability volume $\tilde{\Omega}$ (centered at $\mathbf{x}$) in nanoindentation with a smooth indenter is usually localized inside the material without the direct contact with the external indenter,[7,24,25] and its size increases with a decreasing local strain gradient $\nabla\mathbf{E}$.[26] When $\nabla\mathbf{E}$ is rather small, the atomic configuration in $\tilde{\Omega}$ approaches that of Θ, and the size of $\tilde{\Omega}$ would be significantly greater than the cutoff radius of the interatomic potential. It thus allows us, with diminishing error, to inspect the lattice stability of the infinite and homogeneously strained Θ instead of the inhomogeneous counterpart. To achieve this, development of new efficient algorithm is required, because in principle all the phonons in the full BZ ($\mathbf{k}$ space) of Θ for every material point within $\mathbf{x}$ space should be treated.

On the other hand, even if the soft phonons could be effectively pinpointed in crystals, it is still challenging to predict the final defect configuration. The unstable phonon mode indicates only the initial linear instability of atomic displacements, and as nonlinear effects develop, it becomes invalid as a descriptor at finite amplitude.[15] In addition, a phonon is delocalized, and even a soft-phonon wave packet would span many atomic planes, whereas a defect such as a dislocation is localized down to one plane,[26] implying that there should be a localization process during the evolution of a soft-phonon pack prior to defect nucleation. For a long-wave soft phonon, the localization process into a dislocation loop has been demonstrated.[7,8] Although the

[1]School of Materials Science and Engineering, Shanghai Jiao Tong University, Shanghai, China; [2]Department of Nuclear Science and Engineering, Massachusetts Institute of Technology, Cambridge, MA, USA and [3]Department of Materials Science and Engineering, Massachusetts Institute of Technology, Cambridge, MA, USA
Correspondence: Professor J Gu, School of Materials Science and Engineering, Shanghai Jiao Tong University, 800 Dongchuan Road, Shanghai 200240, China.
E-mail: gujf@sjtu.edu.cn
or Professor J Li, Department of Nuclear Science and Engineering, Massachusetts Institute of Technology, 77 Massachusetts Avenue, Room 24-202, Cambridge, MA 02139, USA.
E-mail: liju@mit.edu
Received 23 April 2016; revised 5 July 2016; accepted 20 July 2016

softening of finite-**k** phonons, particularly, the zone-boundary phonons, is quite common in shape-memory alloys,[27] ferroelectric compounds[28] and two-dimensional materials,[18,20,23] their dynamical evolutions have not been previously reported.

In this paper, we develop a fast and robust full-BZ soft-phonon-searching algorithm called *Phorion*. Combining finite-element modeling incorporating *Phorion* and atomistic simulations, we show how a zone-boundary phonon instability is first triggered in a simple metal (aluminum) under nanoindentation and how it metamorphoses into a deformation twin (DT). We propose a general mechanism that governs the dynamical transformation of the soft short-wave phonons.

MATERIALS AND METHODS

Full-BZ soft-phonon-searching algorithm: *Phorion*

We design *Phorion* to capture soft phonons in the joint material-reciprocal (**x**–**k**) spaces, in which the positioning of the 'softest' phonon is treated as a linearly constrained optimization problem:

$$\begin{aligned} &\min_{\mathbf{x},\mathbf{k}} f(\mathbf{x},\mathbf{k}) \equiv \omega^2/|\mathbf{k}|^2 \\ &\text{s.t.} \quad \mathbf{A}_1\cdot\mathbf{x} \leqslant \mathbf{b}_1 \\ &\qquad \mathbf{A}_2\cdot\mathbf{k} \leqslant \mathbf{b}_2 \end{aligned} \tag{1}$$

where **x** and **k** are constrained within the sample volume and the first BZ, respectively; ω is calculated by diagonalizing the **k**-dependent dynamical matrix and taking the lowest eigenvalue at each location **x** with the finite strain. The objective function f is set as $\omega^2/|\mathbf{k}|^2$ rather than ω^2 to prevent the minimum f ($f_{\min}$) from being always pinned at the Γ point in the BZ during minimization. Obviously, once $f_{\min}$ is detected to first hit zero at ($\mathbf{x}^*$, $\mathbf{k}^*$) during the load ramp, the position $\mathbf{x}^*$ and wave vector $\mathbf{k}^*$, as well as the polarization vector $\mathbf{w}^*$ of the soft phonon can be determined. Because there exist multiple local minima for the linearly constrained optimization problem, we implement an effective strategy to capture the global minimum reliably and efficiently by taking and utilizing the analytical gradients of Equation (1) (see Supplementary Sec. I for details).

Finite-element modeling

We seamlessly incorporate *Phorion* into the interatomic potential finite-element model (IPFEM),[7,19] an extended local version of the quasicontinuum method.[29] We then use the IPFEM-*Phorion* approach to simulate a cylindrical (111) indentation of a single crystal Al plate and pinpoint the phonon instability within the joint **x**–**k** space at 0 K. IPFEM simulation of nanoindentation is performed using the commercial finite-element software ABAQUS (Dassault Systèmes, Vélizy-Villacoublay, France) by writing the UMAT subroutine, with the Zope–Mishin embedded-atom method (EAM) potential of Al[30] as the atomistic constitutive input. A single crystal Al plate, oriented as $x[11\bar{2}] - y[111] - z[1\bar{1}0]$ with a size of 2000 × 1000 Å in the x–y plane, is indented on its top surface of the (111) plane at 0 K by an analytical rigid cylindrical indenter with a radius of 500 Å lying along $z[1\bar{1}0]$. The finite-element model, divided into 130 592 linear plane-strain elements, is free on the top surface, and is fixed at the bottom and in the x direction on both sides. The indentation proceeds in a displacement control with an indentation depth of 0.1 Å per step. *Phorion* is invoked at the end of each step.

Atomistic simulation

We use the LAMMPS code[31] to perform the molecular dynamics (MD) simulation of nanoindentation. The size and boundary conditions of the indented Al plate in the x–y plane as well as the interatomic potential are the same as those in IPFEM simulation. PBC is applied in z, with half of the

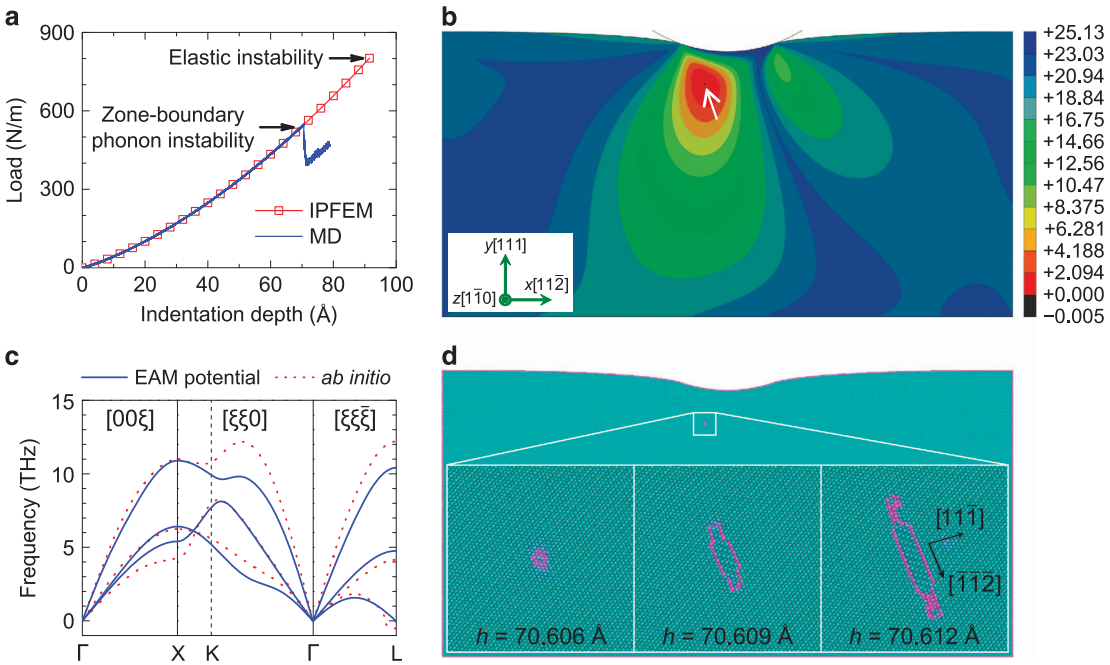

Figure 1 IPFEM-*Phorion* and MD simulations of (111) cylindrical nanoindentation of Al. The size of the Al plate in x–y plane is 2000 × 1000 Å and the indenter radius is 500 Å. (**a**) Load (P) versus indentation depth (h) by IPFEM and MD simulations. *Phorion* and the acoustic tensor formalism embedded in IPFEM predict a zone-boundary phonon instability and an elastic instability occurring at h = 69.7 and 91.5 Å, respectively. (**b**) Contour of the objective function f in Equation (1) at h = 69.7 Å by IPFEM-*Phorion* simulation, in which the wave vector **k** is fixed at $[11\bar{1}]/2$. Homogeneous lattice instability site is indicated by the arrow, where f vanishes first at 184.6 Å beneath the top surface and 79.0 Å away from the central y axis. (**c**) Phonon spectra of the Al crystal lattice strained according to the local deformation gradient of the predicted lattice instability site shown in (**b**), based on the Zope–Mishin Al EAM potential (blue solid) and *ab initio* calculation using the Goedecker–Teter–Hutter Al pseudopotential (red dot). Both predict an acoustic phonon branch softening at $L = [11\bar{1}]/2$, with a polarization displacement vector $\mathbf{w}^*//[\bar{1}10]$. (**d**) Atomic configurations at the early stages of DT nucleation by MD simulation. Insets show magnified snapshots of how the DT is homogeneously nucleated. DT embryo center is positioned at 186.9 Å beneath the top surface and 80.7 Å displaced from the central y axis. Atoms are colored according to the central symmetric parameter.[24] IPFEM, interatomic potential finite-element model; MD, molecular dynamics.

thickness greater than the cutoff radius given by the Zope–Mishin potential. About two million atoms are contained in the simulation box. Following ref. 24, nanoindentation is implemented by introducing an external repulsive potential acting upon the atoms on the top surface with a force constant of 10 eV Å^{-3}; this virtual indenter proceeds at a speed of 1 m s^{-1}. The time step is 1 fs, and the temperature is controlled at 1 K using an NVT ensemble with the Nosé–Hoover thermostat.[32,33]

Ab initio calculation

To verify that the soft phonon predicted by IPFEM-*Phorion* based on the Zope–Mishin potential is real, we use the ABINIT code[34] to perform an *ab initio* calculation of the phonon spectra of the homogeneously strained lattice at the predicted instability site. The Goedecker–Teter–Hutter Al pseudopotential is adopted within the local density approximation[35–37] with a 20 Ha energy cutoff. Marzari's 'cold-smearing' method[38] is used for BZ integrations with a smearing parameter of 0.04 Ha. The lattice constant a_0 of Al is first obtained using a $12\times12\times12$ Monkhorst–Pack[39] k-point grid and is found to be 3.99 Å, in good agreement with the experimental 4.03 Å[40] value and the 4.05 Å value given by the Zope–Mishin potential. The Al lattice with the calculated a_0 is then subjected to a homogeneous strain according to the local deformation gradient at the IPFEM-*Phorion*-predicted instability site; the phonon frequencies of which are calculated using the density functional perturbation theory[41] with a $20\times20\times20$ Monkhorst–Pack k-point grid.

RESULTS AND DISCUSSION

Figure 1a shows the indentation load (P) versus the indentation depth (h) response from the IPFEM simulation. With remarkable computational efficiency (Supplementary Sec. I), *Phorion* predicts that a zone-boundary phonon instability occurs inside the crystal at $h=69.7$ Å (Figure 1b), with a local Mises shear stress as large as 12.1 GPa. Examination of the phonon dispersion at the instability site based on the Zope–Mishin potential (Figure 1c) shows that a transverse acoustic phonon branch softens at L with a wave vector $\mathbf{k}^*$ of $[11\bar{1}]/2$ and polarization vector $\mathbf{w}^*//[\bar{1}10]$. This soft mode is also verified by the *ab initio* calculation. To compare, we also utilize the acoustic tensor formalism[42,43] (equivalent to the Λ criterion[7]) within IPFEM to predict the onset of elastic (long-wave) instability. As shown in Figure 1a, the critical h is predicted to be 91.5 Å, occurring much later than the zone-boundary phonon instability. Moreover, the instability position and the mode are also different (Supplementary Figure S4).

To verify the bi-continuum prediction (joint $\mathbf{x}-\mathbf{k}$ space), we have carried out direct MD simulation using the same empirical potential. As shown in Figure 1a, the P–h curves obtained by MD and IPFEM simulations agree very well before the first load drop in MD, and the critical h of 70.6 Å is very close to that predicted by *Phorion*, whereas the prediction by the $\mathbf{k}\approx0$ acoustic tensor criterion lags far behind. In MD, the load drop is found to correspond to the homogeneous nucleation of a DT, and the position of the DT embryo center agrees nearly perfectly with *Phorion*'s prediction (Figure 1d). The observed twinning plane of $(11\bar{1})$ is consistent with $\mathbf{k}^*$ provided by *Phorion*. However, the DT shear strain direction, which is $[\bar{1}\bar{1}2]$, differs from the phonon polarization direction $\mathbf{w}^*//[\bar{1}10]$; indeed, the two are perpendicular. This deviates greatly from the previous understanding for long-wave soft phonons.[8] We also note a curious fact that the phonon-predicted ($\mathbf{k}^*$, $\mathbf{w}^*$) shear between adjacent atomic planes has zero Schmid factor in Figure 1b, so no mechanical work can be conducted during the initial bifurcation instability. It is then intriguing to connect the predicted soft-phonon mode with the homogeneous nucleation of the DT embryo.

To unravel this continuum-atomic connection, we perform a focused analysis of the evolution of *Phorion*-pinpointed soft phonon by direct MD simulation. First, an Al supercell under PBC is created with a homogeneous strain according to the local deformation gradient tensor at the instability site (Figure 1b), as shown in Figure 2a. It is oriented such that its x and z axes are along the soft phonon's $\mathbf{w}^*//[\bar{1}10]$ and $\mathbf{k}^*//(11\bar{1})$ plane normal, respectively. A low-amplitude (perturbational), high-wave vector atomic displacement wave according to the soft phonon's polarization is then injected into the supercell (Figure 2a). Its ultrafast evolution dynamics are then traced directly with MD. Figure 2b shows the evolution of the perturbational wave prior to defect nucleation. It can be observed that, instead of continuous growth, the wave experiences an amplitude oscillation while keeping its original shape up to ~19.8 ps (Figure 2b I–IV). Then its upper and lower envelopes bend into sinusoidal shapes, and their amplitudes continue to grow until ~23.5 ps (Figure 2b V–VI). Finally, the envelope curves evolve into a defect embryo residing in only a couple of atomic layers and forms a conspicuous displacement shuffling along $x[\bar{1}10]$ within the packet (Figure 2b VII–VIII).

To understand the zone-boundary phonon driven process above, we analyze the temporal evolution of the displacement in x (u_x) of each $(11\bar{1})$ atomic layer. As shown in Figure 2c, we may divide the odd- and even-numbered $(11\bar{1})$ atomic layers into A_1 and A_2 groups,

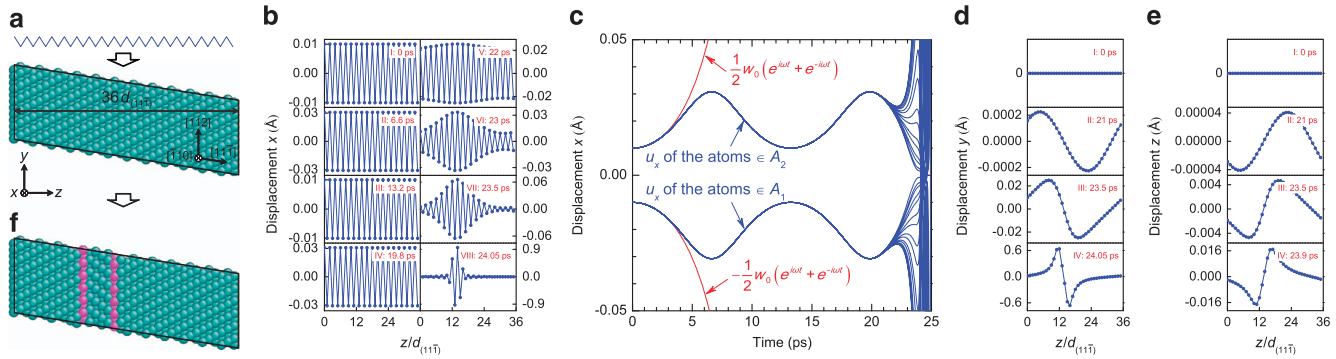

Figure 2 Structural metamorphosis of a perturbed Al supercell. (**a**) Al supercell under PBCs is subjected to the same strain as that at the lattice instability site predicted by *Phorion* shown in Figure 1b. It is perturbed by a plane wave according to the instability mode of the soft L phonon shown in Figure 1c, with an initial amplitude w_0 of 0.01 Å. (**b**, **d** and **e**) Spatial evolutions of the displacements of the 36 $(11\bar{1})$ atomic layers along x, y and z, respectively. (**c**) Temporal evolution of the displacements x of the $(11\bar{1})$ atomic layers (in blue), which are initially bunched together in two groups, A_1 and A_2. They are compared with the linear exponential growth curves (in red), in which the L phonon's imaginary circular frequency $\omega=0.406i$ THz. (**f**) Atomic configuration of the supercell at 24.05 ps, in which a deformation twin is nucleated. Atoms are colored according to the central symmetry parameter, with red atoms constituting two twinning planes. PBC, periodical boundary condition.

in which their u_x are initially bunched together, thereby being grouped into the initial lower- and upper-straight envelope lines. Such bunching is maintained until ~19.8 ps, accounting for the undistortion of the wave profile shown in Figure 2b I–IV. During this stage, u_x of A_1 and A_2 groups first follow linear exponential growth as $u_x(t) = \mp\frac{1}{2}w_0\left(e^{i\omega t} + e^{-i\omega t}\right)$ with an imaginary ω within the harmonic approximation, where w_0 is the initial amplitude of the perturbational wave. However, they then deviate from this pure amplitude growth and start to oscillate. Such a response is attributed to the anharmonic terms in the total potential energy expansion $\Delta\Psi = c_2u_A^2 + c_4u_A^4 + \cdots$, where u_A is the phonon displacement. The lack of the cubic term is owing to the symmetry of the zone-boundary phonon mode (see Supplementary Sec. III for the analytical expressions of $\Delta\Psi$). Figure 3 compares $\Delta\Psi - u_A$ of the harmonic expansion with that including the fourth-order anharmonic term. In contrast to a downward parabola of the harmonic expansion, the significant anharmonic effect yields a double-well potential, which in principle could arrest the perturbational wave and suppress the amplitude growth. The behavior of the injected wave in stages I–IV in Figure 2b could thus be understood. Indeed, using the Landau polynomials language of phase transitions, what Figure 3 describes is a phase transformation that should occur after the *L*-phonon 'spinodal' instability (in displacement, instead of chemical concentration) to a new crystal structure. In Figure 3, adjacent $(11\bar{1})$ atomic layers undergo displacement shuffling along $[\bar{1}10]$ on the path from the center to one of the double wells, which is actually accompanied by a phase transformation from the original face-centered cubic (FCC) phase to a new triclinic (TRI) phase. As shown in the primitive cell of the TRI structure, there exist two basis atoms occupying two sites (denoted as B_1 and B_2) on adjacent $(11\bar{1})$ atomic layers that exactly belong to the A_1 and A_2 groups, respectively.

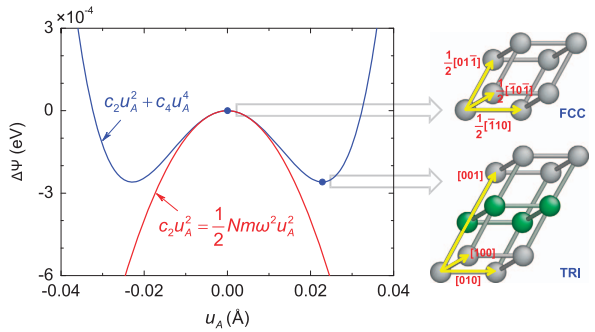

Figure 3 Response of the potential energy change ($\Delta\Psi$) of the Al supercell to the phonon displacement (u_A) of the perturbational wave. $\Delta\Psi$ can be fitted as $c_2u_A^2 + c_4u_A^4$ (in blue), where $c_2 = -0.993$ eV Å^{-2} and $c_4 = -949.7$ eV Å^{-4}, compared with the harmonic-approximation response following $\Delta\Psi = c_2u_A^2 = \frac{1}{2}Nm\omega^2u_A^2$ (in red), where N is the number of atoms in the supercell and m is the atomic mass of Al. Primitive cells of the FCC and TRI structures, corresponding to the center and the bottom of the double wells, respectively, are shown on the right, and they have $d^{TRI}_{(001)} = 2d^{FCC}_{(11\bar{1})}$. Two basis atoms in the TRI primitive cell are colored with gray and green, respectively. TRI, triclinic.

However, this phase transformation, triggered by the zone-boundary soft phonon, does not significantly relax the strain energy, and the TRI phase is still subjected to high stress. Therefore, it is still necessary to keep inspecting its structural instability. If the TRI structure were mechanically stable, the injected perturbational and subsequently grown wave could be dissipated by phonon scattering[44] and permanently arrested by the double-well potential, which would lead to a polymorphic phase transition such as those observed in some indentation experiments.[45,46] Otherwise, the second-generation lattice instability within the TRI structure would affect the wave growth and may drive it to escape from the TRI phase in a different direction not reflected in the Landau polynomial plot of Figure 3.

In fact, second-generation phonon spectra analysis shows that the TRI structure is elastically unstable for a long wave with $\mathbf{k}//[001]^{TRI}$ (Figure 4a), where $[001]^{TRI}$ is a reciprocal vector to the real-space lattice vectors of TRI shown in Figure 3. For the present supercell with a limited size along z, only a soft phonon with $\mathbf{k}$ of $[001]^{TRI}/18$ is allowed to be excited and is expected to generate two independent unstable long waves denoted as β_1 and β_2 that involve the collective movement of the B_1- and B_2-sited (or A_1- and A_2-grouped) atoms, respectively. Eigenmode analysis shows that each of the long waves can be decomposed into three polarization components including two transverse waves β_i^x and β_i^y oscillating along x and y, respectively, and a longitudinal wave β_i^z oscillating along z ($i = 1, 2$), with their normalized amplitudes v and phase φ shown in Supplementary Table S3. As the displacement shuffling along $[\bar{1}10]$ breaks the central symmetry of B_1- and B_2-sited atoms in the TRI structure, these

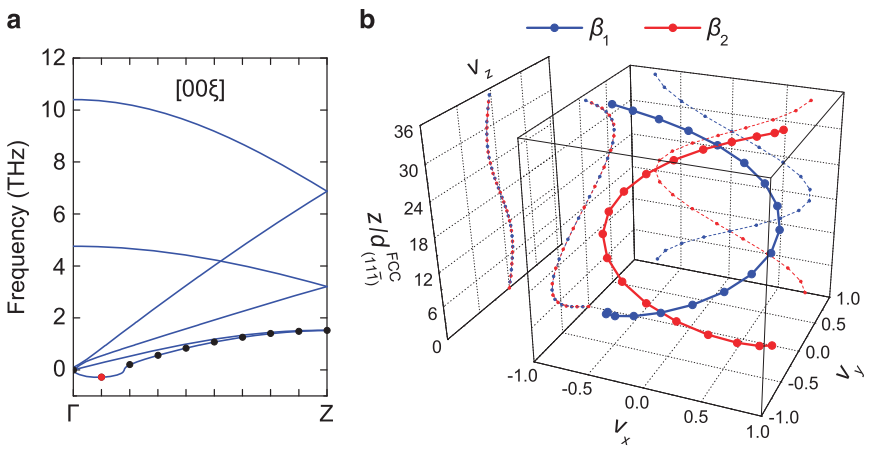

Figure 4 Near-Γ phonon instability of the TRI structure. (**a**) Phonon spectra of the TRI structure along the Γ-*Z* path in the BZ. For the present supercell with $l_z = 18d^{TRI}_{(001)}$, there are nine *k* points allowable distributed uniformly between (Γ, *Z*], of which the frequencies on the softened phonon branch are denoted as solid dots. Among these, only the *k* point at $[001]^{TRI}/18$ has an imaginary frequency, denoted as the red dot. (**b**) Wave profiles with normalized amplitudes of two unstable long waves β_1 and β_2 excited by the soft phonon denoted in (**a**). Two long waves spatially constitute a double helix, with their polarization components shown on the projective planes. BZ, Brillouin zone; TRI, triclinic.

polarization components have different phases, yielding a double-helix profile for the β_1–β_2 pair (Figure 4b). For the β_1^x and β_2^x waves, owing to a phase difference of π, their superposition upon the original injected wave would bend its lower and upper envelope lines into a pair of sinusoidal curves oscillating oppositely and coherently, and drive the system to escape from the double-well potential; this explains the profile of the injected wave shown in Figure 2b V. The continuous amplitude growth of the sinusoidal envelope curves (Figure 2b VI) followed by progressive localization (Figure 2b VII–VIII) agrees well with the localization behavior of an unstable elastic wave,[8] even though 'wave-front steepening' that breaks the positive strain–negative strain symmetry is not observed, resulting from the vanishing shear stress component $\tau_{zx}=0$ (zero Schmid factor) here.

As indicated above, the TRI structure would also generate polarization components oscillating along y and z, which contribute to the DT nucleation as well. For the β_1^y and β_2^y waves with the same ν and φ (Supplementary Table S3), they are expected to be merged into a single long wave β^y with phase $\pi/2$ ahead of β_1^x, involving collective displacements along y of all the A_1- and A_2-grouped atoms. Such a prediction is verified by tracing the evolution of u_y for all the $(11\bar{1})$ atomic layers, shown in Figure 2d. It can be observed that a single long u_y wave is excited, followed by the amplitude growth (Figure 2d I–II), wave-front steepening (Figure 2d III), and shrinking into a couple of atomic layers and thus producing a uniform shear along $[\bar{1}\bar{1}2]$ (Figure 2d IV); this wave actually behaves as an unstable elastic wave.[8] Simultaneously, a single u_z wave also develops owing to crystallographic shear-tension coupling[8] and experiences the dynamics similar to those of the u_y wave (Figure 2e), albeit with much smaller amplitude.

Therefore, eventually, the TRI phase turns out to be just an intermediate product, decomposing within tens of picoseconds by the second-stage, near-Γ phonon instability to evolve into a lattice defect–DT, as shown in Figure 2f. Its atomic structure is verified to be consistent with that in Figure 1d, proving the continuum-atomic linkage and the validity of our bi-continuum prediction (joint $\mathbf{x}-\mathbf{k}$ space) as well as focal study of nucleation dynamics with PBCs. Unexpectedly, and quite distinct from a conventional DT in which all atomic planes slip along the same direction (same Shockley partial Burgers vector) thereby producing a uniform shear strain, the DTs in Figure 1d and 2f have two different slip vectors alternating along $[1\bar{2}\bar{1}]$ and $[\bar{2}1\bar{1}]$ on every successive $(11\bar{1})$ planes. In fact, our DT embryo is mainly achieved by the superposition of the displacement shuffling along $[\bar{1}10]$ resulting from the localization of the β_1^x and β_2^x waves, and the shear strain along $[\bar{1}\bar{1}2]$ contributed by the accumulated deformation before the L-phonon softening plus the localization of the β^y wave (β^z contribution can be neglected owing to a small amplitude). The two slip vectors are produced through $\pm\frac{1}{4}[1\bar{1}0]+\frac{1}{12}[\bar{1}\bar{1}2]=\frac{1}{6}[1\bar{2}\bar{1}]$ and $\frac{1}{6}[\bar{2}1\bar{1}]$ for adjacent $(11\bar{1})$ planes, and the stacking order is thus changed from the original '$\cdots ABCABCAB\cdots$', for example, to '$\cdots A|\boldsymbol{B}ACBA\boldsymbol{C}|A\cdots$'. In other words, a DT with a width of $5d_{(11\bar{1})}$ nucleates homogeneously in the lattice (see Supplementary Figure S5 for the schematic of how the stacking order is changed). If viewed from $[1\bar{1}0]$, the DT has an averaged transformation shear along $[\bar{1}\bar{1}2]$, where the average relative slip vector between two adjacent $(11\bar{1})$ planes is $\frac{1}{12}[\bar{1}\bar{1}2]$, only 50% of that of the conventional textbook DT (Supplementary Figure S6), leading to a significantly smaller transformation strain and smaller elastic energy of embedding. Interestingly, our DT embryo shows a crude resemblance to the DT growing from a grain boundary following a dislocation-reaction and cross-slip mechanism recently proposed by Zhu *et al.*,[47,48] which also incorporates two different slip vectors or alternating Shockley partial Burgers vectors. To be revealed as the product of two degenerate soft phonons is quite a surprise, though.

CONCLUSIONS

In summary, we have developed a robust full-BZ soft-phonon-searching algorithm, which can be combined with other multiscale simulation methods or *ab initio* calculation tools to predict the lattice instability and the ideal strength of materials that enable elastic strain engineering.[1] We have revealed how a continuum soft phonon evolves into a discrete atomic defect within tens of picoseconds in an indented perfect crystal at stress extreme. This involves four stages: (1) linear growth of an unstable short wave triggered by a softened L phonon, well described by the harmonic-approximation phonon theory; (2) arrest of the short wave by a double-well potential in the form of an anharmonic Landau polynomial, indicating a polymorphic phase transformation from FCC to TRI; (3) excitation of two independent unstable long waves by a soft near-Γ phonon in the TRI lattice; and (4) growth and localization of the two long waves until trapped in a couple of atomic layers, where an unconventional DT embryo with staggered slip Burgers vectors and 50% of the total transformation strain of the textbook FCC DT is formed. In this two-stage soft-phonon cascade, the Landau polynomial has a critical role, with the anharmonic energy terms arresting the dynamics of an L phonon in FCC followed by a near-Γ phonon in TRI. In Supplementary Sec. IV, we show an analytical scaling theory that explains why an unstable long elastic wave is much more difficult to be trapped in a polynomial energy landscape.

The Figure 3 scenario is not unlike the well-known temperature-driven phase transformation within a double-well potential[49] in phonon coordinate. However, a salient feature of the stress-driven martensitic transformation owing to a softened zone-boundary phonon is that the new phase still withstands high stress, and it is thus highly likely to be unstable as well and prone to the next-stage evolution. This is because a first-generation transition yields little transformation strain, as the zone-boundary phonon has too short wavelength, unlike a long-wavelength phonon that can significantly relax the strain in a local region. In view of this, we believe that the proposed two-stage transformation mechanism can generally describe the dynamics of the homogeneous defect nucleation induced by a softened zone-boundary (or nearby) phonon at stress extremes. As we show in Supplementary Sec. V, it can also fully account for the homogeneous nucleation of a dislocation. The general utility of IPFEM-*Phorion* bi-continuum stability analysis has been repeatedly verified by our direct atomistic simulations. The uncovered material dynamics at stress extremes reveal deep connections between delocalized phonons in $\mathbf{x}$ and $\mathbf{k}$ continua—a wave phenomenon controlled by the harmonic part of potential—and localized atomic defects trapped by the full nonlinear interatomic potential energy landscape, which adds to the rich repertoire of nonlinear dynamics found in nature.[50,51]

CONFLICT OF INTEREST

The authors declare no conflict of interest.

ACKNOWLEDGEMENTS

This work was supported by the Natural Science Foundation of China under Grant Nos. 50971090, 51071102, 51201101 and 51471107. JL acknowledges the support of NSF DMR-1410636. XL acknowledges helpful discussion with M.H. Wu about the *ab initio* calculation of phonon spectra.

1 Li, J., Shan, Z. W. & Ma, E. Elastic strain engineering for unprecedented materials properties. *MRS Bull.* **39**, 108–117 (2014).
2 Feng, J., Qian, X., Huang, C.-W. & Li, J. Strain-engineered artificial atom as a broad-spectrum solar energy funnel. *Nat. Photonics* **6**, 866–872 (2012).
3 Li, H., Contryman, A. W., Qian, X., Ardakani, S. M., Gong, Y., Wang, X., Weisse, J. M., Lee, C. H., Zhao, J., Ajayan, P. M., Li, J., Manoharan, H. C. & Zheng, X. Optoelectronic crystal of artificial atoms in strain-textured molybdenum disulphide. *Nat. Commun.* **6**, 7381 (2015).
4 Hao, S., Cui, L., Wang, H., Jiang, D., Liu, Y., Yan, J., Ren, Y., Han, X., Brown, D. E. & Li, J. Retaining large and adjustable elastic strains of kilogram-scale Nb nanowires. *ACS Appl. Mat. Interfaces* **8**, 2917–2922 (2016).
5 Liu, F., Ming, P. M. & Li, J. *Ab initio* calculation of ideal strength and phonon instability of graphene under tension. *Phys. Rev. B* **76**, 064120 (2007).
6 Zhu, T. & Li, J. Ultra-strength materials. *Prog. Mater. Sci.* **55**, 710–757 (2010).
7 Li, J., Van Vliet, K. J., Zhu, T., Yip, S. & Suresh, S. Atomistic mechanisms governing elastic limit and incipient plasticity in crystals. *Nature* **418**, 307–310 (2002).
8 Li, J., Ngan, A. H. W. & Gumbsch, P. Atomistic modeling of mechanical behavior. *Acta Mater.* **51**, 5711–5742 (2003).
9 Van Vliet, K. J., Li, J., Zhu, T., Yip, S. & Suresh, S. Quantifying the early stages of plasticity through nanoscale experiments and simulations. *Phys. Rev. B* **67**, 104105 (2003).
10 Zhu, T., Li, J., Van Vliet, K. J., Ogata, S., Yip, S. & Suresh, S. Predictive modeling of nanoindentation-induced homogeneous dislocation nucleation in copper. *J. Mech. Phys. Solids* **52**, 691–724 (2004).
11 Fago, M., Hayes, R. L., Carter, E. A. & Ortiz, M. Density-functional-theory-based local quasicontinuum method: prediction of dislocation nucleation. *Phys. Rev. B* **70**, 100102 (2004).
12 Liu, X. H., Gu, J. F., Shen, Y. & Chen, C. F. Anisotropy in homogeneous dislocation nucleation by nanoindentation of single crystal Cu. *Scripta Mater.* **58**, 564–567 (2008).
13 Einarsdotter, K., Sadigh, B., Grimvall, G. & Ozoliņš, V. Phonon instabilities in fcc and bcc Tungsten. *Phys. Rev. Lett.* **79**, 2073–2076 (1997).
14 Li, J. & Yip, S. Atomistic measures of materials strength. *Comput. Model. Eng. Sci.* **3**, 219–227 (2002).
15 Clatterbuck, D. M., Krenn, C. R., Cohen, M. L. & Morris, J. W. Phonon instabilities and the ideal strength of aluminum. *Phys. Rev. Lett.* **91**, 135501 (2003).
16 Dmitriev, S. V., Li, J., Yoshikawa, N. & Shibutani, Y. Theoretical strength of 2D hexagonal crystals: application to bubble raft indentation. *Philos. Mag.* **85**, 2177–2195 (2005).
17 Dubois, S. M. M., Rignanese, G. M., Pardoen, T. & Charlier, J. C. Ideal strength of silicon: an *ab initio* study. *Phys. Rev. B* **74**, 235203 (2006).
18 Marianetti, C. A. & Yevick, H. G. Failure mechanisms of graphene under tension. *Phys. Rev. Lett.* **105**, 245502 (2010).
19 Liu, X. H., Gu, J. F., Shen, Y., Li, J. & Chen, C. F. Lattice dynamical finite-element method. *Acta Mater.* **58**, 510–523 (2010).
20 Li, T. Ideal strength and phonon instability in single-layer MoS_2. *Phys. Rev. B* **85**, 235407 (2012).
21 Grimvall, G., Magyari-Köpe, B., Ozoliņš, V. & Persson, K. A. Lattice instabilities in metallic elements. *Rev. Mod. Phys.* **84**, 945–986 (2012).
22 Zhou, W., Zhang, Y., Sun, H. & Chen, C. Ideal strength and structural instability of aluminum at finite temperatures. *Phys. Rev. B* **86**, 054118 (2012).
23 Isaacs, E. B. & Marianetti, C. A. Ideal strength and phonon instability of strained monolayer materials. *Phys. Rev. B* **89**, 184111 (2014).
24 Kelchner, C. L., Plimpton, S. J. & Hamilton, J. C. Dislocation nucleation and defect structure during surface indentation. *Phys. Rev. B* **58**, 11085–11088 (1998).
25 Gouldstone, A., Van Vliet, K. J. & Suresh, S. Nanoindentation—simulation of defect nucleation in a crystal. *Nature* **411**, 656–656 (2001).
26 Miller, R. E. & Rodney, D. On the nonlocal nature of dislocation nucleation during nanoindentation. *J. Mech. Phys. Solids* **56**, 1203–1223 (2008).
27 Otsuka, K. & Ren, X. Physical metallurgy of Ti-Ni-based shape memory alloys. *Prog. Mater. Sci.* **50**, 511–678 (2005).
28 Blinc, R. & Zeks, B. *Soft Modes in Ferroelectrics and Antiferroelectrics* (Elsevier, New York, NY, USA, 1974).
29 Tadmor, E. B., Ortiz, M. & Phillips, R. Quasicontinuum analysis of defects in solids. *Philos. Mag. A* **73**, 1529–1563 1996).
30 Zope, R. R. & Mishin, Y. Interatomic potentials for atomistic simulations of the Ti-Al system. *Phys. Rev. B* **68**, 241021–2410214 (2003).
31 Plimpton, S. Fast parallel algorithms for short-range molecular dynamics. *J. Comput. Phys.* **117**, 1–19 (1995).
32 Nosé, S. A unified formulation of the constant temperature molecular dynamics methods. *J. Chem. Phys.* **81**, 511–519 (1984).
33 Hoover, W. G. Canonical dynamics: equilibrium phase-space distributions. *Phys. Rev. A* **31**, 1695–1697 (1985).
34 Gonze, X., Beuken, J.-M., Caracas, R., Detraux, F., Fuchs, M., Rignanese, G.-M., Sindic, L., Verstraete, M., Zerah, G., Jollet, F., Torrent, M., Roy, A., Mikami, M., Ghosez, Ph., Raty, J.-Y. & Allan, D. C. First-principles computation of material properties: the ABINIT software project. *Comput. Mater. Sci.* **25**, 478–492 (2002).
35 Ceperley, D. M. & Alder, B. J. Ground state of the electron gas by a stochastic method. *Phys. Rev. Lett.* **45**, 566–569 (1980).
36 Perdew, J. P. & Wang, Y. Accurate and simple analytic representation of the electron-gas correlation energy. *Phys. Rev. B* **45**, 13244–13249 (1992).
37 Goedecker, S., Teter, M. & Hutter, J. Separable dual-space Gaussian pseudopotentials. *Phys. Rev. B* **54**, 1703–1710 (1996).
38 Marzari, N. *Ab-initio Molecular Dynamics for Metallic Systems* (University of Cambridge, 1996).
39 Monkhorst, H. J. & Pack, J. D. Special points for Brillouin-zone integrations. *Phys. Rev. B* **13**, 5188–5192 (1976).
40 Eisenmann, B., Schäfer, H., Landolt-Börnstein. in *Structure Data of Elements and Intermetallic Phases. Elements, Borides, Carbides, Hybrides* (eds Hellwege K.-H. & Hellwege A. M.) (Springer-Verlag, New York, NY, USA, 1988).
41 Baroni, S., de Gironcoli, S., Dal Corso, A. & Giannozzi, P. Phonons and related crystal properties from density-functional perturbation theory. *Rev. Mod. Phys.* **73**, 515 (2001).
42 Hill, R. Acceleration waves in solids. *J. Mech. Phys. Solids* **10**, 1–16 (1962).
43 Rice, J. R. in *Theoretical and Applied Mechanics* (ed. Koiter W. T.) Vol. 1, 207–220 (North-Holland, Amsterdam, The Netherlands, 1976).
44 Li, J., Porter, L. & Yip, S, Atomistic modeling of finite-temperature properties of crystalline β-SiC: II. Thermal conductivity and effects of point defects. *J. Nucl. Mater.* **255**, 139–152 (1998).
45 Pharr, G. M., Oliver, W. C. & Harding, D. S. New evidence for a pressure-induced phase-transformation during the indentation of silicon. *J. Mater. Res.* **6**, 1129–1130 (1991).
46 Jang, J. I., Lance, M. J., Wen, S. Q. & Pharr, G. M. Evidence for nanoindentation-induced phase transformations in germanium. *Appl. Phys. Lett.* **86**, 131907 (2005).
47 Zhu, Y. T., Wu, X. L., Liao, X. Z., Narayan, J., Mathaudhu, S. N. & Kecskés, L. J. Twinning partial multiplication at grain boundary in nanocrystalline fcc metals. *Appl. Phys. Lett.* **95**, 031909 (2009).
48 Zhu, Y. T., Liao, X. Z. & Wu, X. L. Deformation twinning in nanocrystalline materials. *Prog. Mater. Sci.* **57**, 1–62 (2012).
49 Landau, L. D. & Lifshitz, E. M. *Statistical Physics* (Elsevier Science, 2013).
50 Thompson, J. M. T. & Stewart, H. B. *Nonlinear Dynamics and Chaos* (Wiley, Chichester, UK, 2002).
51 Strogatz, S. H. *Nonlinear Dynamics and Chaos: With Applications to Physics, Biology, Chemistry, and Engineering* (Westview Press, Boulder, CO, USA, 2014).

Supplementary Information accompanies the paper on the NPG Asia Materials website (http://www.nature.com/am)

SUPPLEMENTARY INFORMATION

Crystal Metamorphosis at Stress Extremes: How Soft Phonons Turn into Lattice Defects

Xiaohui Liu[1,2], Jianfeng Gu[1,*], Yao Shen[1], Ju Li[2,3,*]
[1] *School of Materials Science and Engineering, Shanghai Jiao Tong University, Shanghai 200240, China*
[2] *Department of Nuclear Science and Engineering, Massachusetts Institute of Technology, Cambridge, Massachusetts 02139, USA*
[3] *Department of Materials Science and Engineering, Massachusetts Institute of Technology, Cambridge, Massachusetts 02139, USA*
[*] *To whom correspondence should be addressed. E-mail: liju@mit.edu or gujf@sjtu.edu.cn*

CONTENTS

I. FULL-BRILLOUIN ZONE SOFT-PHONON-SEARCHING ALGORITHM: *PHORION*

In this section, we develop a robust full-Brillouin zone (BZ) soft-phonon-searching algorithm termed *Phorion*, which manifests outstanding accuracy and efficiency in positioning phonon instability within the joint **x**-**k** spaces.

As demonstrated by Miller and Rodney recently [1], accurate prediction of lattice instability could be achieved based on eigenmode analysis of the local atomic-scale acoustic tensor. But it is usually cumbersome to get this tensor due to requirement for exact atomic positions and some other preconditions, which further impedes its combination with coarse-grained methods such as the local quasicontinuum (QC) method [2] and the interatomic potential finite-element model (IPFEM) [3, 4]. However, in a slowly varied strain field, as indicated in the main text, it is feasible to turn to examine the structural stability of each infinite lattice that is homogenously strained according to the local deformation of each material point **x**. Homogeneous phonon instability is expected to be located where the local dynamical matrix of the lattice loses positive definiteness first, that is, its lowest eigenvalues ω^2 becomes non-positive. Therefore, the key is to seek the softest phonon with the minimum ω^2 in the joint **x**-**k** spaces. It is straightforward to use the carpet-bombing method to fully scan the **x**-**k** spaces to position the critical point, but it does suffer from the computational cost with power growth of the positioning accuracy [4, 5].

Alternatively, in our developed soft-phonon-searching algorithm *Phorion*, positioning of the softest phonon is treated as a linearly constrained optimization (LCO) problem:

$$\begin{aligned} \min_{\mathbf{x},\mathbf{k}} & f(\mathbf{x},\mathbf{k}) \equiv \omega^2/|\mathbf{k}|^2 \\ \text{s.t. } & \mathbf{A}_1 \cdot \mathbf{x} \leqslant \mathbf{b}_1 \\ & \mathbf{A}_2 \cdot \mathbf{k} \leqslant \mathbf{b}_2, \end{aligned} \tag{1}$$

where **x** and **k** are constrained within the sample volume and the first BZ, respectively, by the two linear constraint conditions with parameters of $(\mathbf{A}_1, \mathbf{b}_1)$ and $(\mathbf{A}_2, \mathbf{b}_2)$. Noteworthy is that f set as $\omega^2/|\mathbf{k}|^2$ rather than ω^2 is to prevent the minimum f ($f_{\min}$) always pinned at the Γ point in the BZ during minimization. Obviously, once $f_{\min}$ is detected to vanish first at $(\mathbf{x}^*, \mathbf{k}^*)$ during load ramp, the position of the homogeneous phonon instability as well as its instability mode can be determined. LCO algorithms such as TOLMIN [6] can be employed to solve Eq. (1), in which the analytical derivatives of f with respect to **x** and **k** are usually expected to be provided.

Firstly, the derivative of f with respect to **x** can be computed as

$$\frac{\partial f}{\partial \mathbf{x}} = \frac{1}{k^2}\frac{\partial \omega^2}{\partial \mathbf{x}} = \frac{1}{k^2}\frac{\partial \omega^2}{\partial \mathbf{F}} : \frac{\partial \mathbf{F}}{\partial \mathbf{x}}, \tag{2}$$

where **F** is the local deformation gradient tensor at **x**. Then consider a crystal with n basis atoms per primitive cell. From the lattice dynamics theory [7], ω^2 for a given **k** corresponds to one of the eigenvalues of the dynamical matrix whose component is given by

$$\mathbf{D}^{\mathbf{k}}\left(a \;\; a'\right) = \frac{1}{\sqrt{m_a m_{a'}}} \sum_A \mathbf{\Phi} \begin{pmatrix} A & \\ a & a' \end{pmatrix} e^{-i\mathbf{k}\cdot\mathbf{X}(A)}, \;\; (a, a' = 1, \ldots, n), \tag{3}$$

where m_a ($m_{a'}$) is the mass of the basis atom a (a'), $\mathbf{X}(A)$ is the coordinates of the primitive cell A in the undeformed configuration, and $\mathbf{\Phi}\left(\begin{smallmatrix} A & \\ a & a' \end{smallmatrix}\right)$ denotes the force constant matrix component with respect to atoms a and a' whose cell indices differ by A. Therefore, Eq. (2) can be further rewritten as

$$\frac{\partial f}{\partial \mathbf{x}} = \frac{1}{k^2}\left\langle \mathbf{e}^{\mathbf{k}} \left| \frac{\partial \mathbf{D}^{\mathbf{k}}}{\partial \mathbf{F}} \right| \mathbf{e}^{\mathbf{k}} \right\rangle : \frac{\partial \mathbf{F}}{\partial \mathbf{x}}, \tag{4}$$

where $\mathbf{e}^{\mathbf{k}}$ is the $3n$ dimensional normalized eigenvector of $\mathbf{D}^{\mathbf{k}}$ associated with the eigenvalue ω^2, and one has

$$\frac{\partial \mathbf{D}^{\mathbf{k}}\left(a \;\; a'\right)}{\partial \mathbf{F}} = \frac{1}{\sqrt{m_a m_{a'}}} \sum_A \frac{\partial \mathbf{\Phi}\begin{pmatrix} A & \\ a & a' \end{pmatrix}}{\partial \mathbf{F}} e^{-i\mathbf{k}\cdot\mathbf{X}(A)}. \tag{5}$$

The third-order tensor $\partial\mathbf{F}/\partial\mathbf{x}$ in Eq. (4) can be directly calculated with finite-difference method incorporating the deformation gradient tensor at **x** and its neighboring material points based on a solved displacement field. And the correlation between $\mathbf{\Phi}\left(\begin{smallmatrix} A & \\ a & a' \end{smallmatrix}\right)$ and **F** in Eq. (5) can be established by the Cauchy-Born hypothesis [8]. The analytical expressions of $\mathbf{\Phi}\left(\begin{smallmatrix} A & \\ a & a' \end{smallmatrix}\right)$ and $\partial\mathbf{\Phi}\left(\begin{smallmatrix} A & \\ a & a' \end{smallmatrix}\right)/\partial\mathbf{F}$ based on the EAM potential [9] are given in Sec. II.

TABLE S1. Time consumptions for searching the phonon instability in Al under nanoindentation by *Phorion* and the conventional carpet-bombing method. The numbers of elements (N_e) in Models I and II are 32648 and 130592, respectively. The positioning accuracy of $\mathbf{k}$ (A_k) for the carpet-bombing method is set to the same as what *Phorion* is able to achieve, which are in the order of 0.1% and 0.01% for Models I and II, respectively. All the time consumptions are normalized by that of *Phorion* in Model I, and the percentages of their occupation of the respective total simulation time are listed in brackets. The time consumptions of *Phorion* are related to the sampling strategy of soft-phonon seekers. Only one fresh seeker is sampled in each step, and even so, the possibilities of failing to position the true phonon instability site in Models I and II are estimated to be less than 10^{-16} and 10^{-11}, respectively. The time consumed for the carpet-bombing method (t_cb) in both models are estimated by using a model with a smaller (N_e) and a larger A_k considering $t_\mathrm{cb} \propto N_\mathrm{e}/A_k^3$.

Model	*Phorion*	Carpet-bombing method
I	1 (2.5%)	1.75×10^{12} ($\sim 100\%$)
II	1.4 (0.7%)	7×10^{15} ($\sim 100\%$)

Similarly, the derivative of f with respect to $\mathbf{k}$ is given by

$$\frac{\partial f}{\partial \mathbf{k}} = \frac{1}{k^2}\frac{\partial \omega^2}{\partial \mathbf{k}} - \frac{2\omega^2 \mathbf{k}}{k^4} = \frac{1}{k^2}\left\langle \mathbf{e}^\mathbf{k} \left| \frac{\partial \mathbf{D}^\mathbf{k}}{\partial \mathbf{k}} \right| \mathbf{e}^\mathbf{k} \right\rangle - \frac{2\omega^2 \mathbf{k}}{k^4}, \tag{6}$$

in which

$$\frac{\partial \mathbf{D}^\mathbf{k}\begin{pmatrix} a & a' \end{pmatrix}}{\partial \mathbf{k}} = \frac{1}{\sqrt{m_a m_{a'}}} \sum_A \mathbf{\Phi}\begin{pmatrix} A & \\ a & a' \end{pmatrix} \otimes \mathbf{X}(A) e^{-i\left[\mathbf{k}\cdot\mathbf{X}(A)+\frac{\pi}{2}\right]}. \tag{7}$$

It is noteworthy that there actually exist multiple local f_{min} in the **x**-**k** spaces. In order to get the global f_min reliably and efficiently, we randomly sample n fresh soft-phonon "seekers" in the **x**-**k** spaces at the end of each step. Driven by TOLMIN, each seeker starts a trip from its initial position and stops till arriving at a local minimum point. The one that gets the lowest local f_min will be inherited to the next step so as to quickly position the new minimum point if it is nearby. Such a strategy incorporating both fresh seekers and inherited seekers guarantees the robustness and efficiency of *Phorion*.

We then evaluate the performance of *Phorion* based on IPFEM-*Phorion* simulations of nanoindentation of Al, and compare it with the conventional "carpet-bombing" method. The Al plate in the main text is employed and divided into two different number of finite elements (Model I and Model II) for comparison. Table S1 lists the time consumptions for searching the phonon instability site in the two models using *Phorion* and the carpet-bombing method. Obviously, the time consumed for the carpet-bombing method is proportional to the number of elements (N_e) used, and grows cubically with the positioning accuracy of $\mathbf{k}$ (A_k). In contrast, that for *Phorion* occupies very little portion of the total simulation time, and is not very sensitive to N_e. In addition, A_k that *Phorion* achieves in both models is within 0.1%. Generally, as can be seen from Table S1, *Phorion* exhibits an overwhelming advantage on computational efficiency over the carpet-bombing method, while possessing high accuracy in positioning the phonon instability. Indeed, *Phorion* can be combined with other multiscale simulation methods or *ab initio* calculation tools to predict phonon instability and ideal strength of materials.

II. ANALYTICAL EXPRESSIONS OF THE FORCE CONSTANT MATRIX AND ITS DERIVATIVE WITH RESPECT TO THE DEFORMATION GRADIENT TENSOR BASED ON THE EAM POTENTIAL

Consider a crystal with n basis atoms per primitive cell. Denote the primitive cells by A and the basis atoms by a, where $a = 1, \ldots, n$. The atoms are indexed by α ($\beta, \gamma, \ldots$), where $\alpha = \binom{A}{a}$ $\left(\beta = \binom{A'}{a'}, \gamma = \binom{A''}{a''}, \ldots\right)$. The force constant matrix component with respect to atoms α and β is given by

$$\mathbf{\Phi}^{\alpha\beta} = \mathbf{\Phi}\begin{pmatrix} A & A' \\ a & a' \end{pmatrix} = \left.\frac{\partial^2 \Psi}{\partial \mathbf{u}^\alpha \partial \mathbf{u}^\beta}\right|_{\mathbf{x}_0}, \tag{8}$$

where Ψ is the total interatomic potential energy of the system, $\mathbf{u}$ is the atomic displacements, and $\mathbf{x}_0$ denotes the equilibrium positions of atoms. As a result of lattice translational symmetry, it has

$$\mathbf{\Phi}\begin{pmatrix} A & A' \\ a & a' \end{pmatrix} = \mathbf{\Phi}\begin{pmatrix} A - A' \\ a & a' \end{pmatrix}, \tag{9}$$

and $\mathbf{\Phi}\left(\begin{smallmatrix} A \\ a\ a' \end{smallmatrix}\right)$ is used to denote the force constant matrix component with respect to atoms a and a' whose cell indices differ by A. Based on the EAM potential [9], Ψ can be expressed as

$$\Psi = \sum_{\alpha} \sum_{\beta \neq \alpha} \frac{1}{2} V^{\alpha\beta}\left(r^{\alpha\beta}\right) + \sum_{\alpha} U^{\alpha}\left(\bar{\rho}^{\alpha}\right). \tag{10}$$

Here $V^{\alpha\beta}$ is the pair potential as a function of distance $r^{\alpha\beta}$ between atoms α and β; U is the embedding energy as a function of the host electron density $\bar{\rho}$, given by

$$\bar{\rho}^{\alpha} = \sum_{\beta \neq \alpha} \rho^{\beta}\left(r^{\alpha\beta}\right), \tag{11}$$

where ρ is the electron density function.

The force constant matrix component with respect to atoms α and β based on the EAM potential can be got by substituting Eq. (10) into Eq. (8), given by

$$\begin{aligned}
\frac{\partial^2 \Psi}{\partial u_i^{\alpha} \partial u_j^{\beta}} = & -\left[\frac{\mathrm{d}^2 V^{\alpha\beta}}{\left(\mathrm{d}r^{\alpha\beta}\right)^2} + \frac{\mathrm{d}U^{\alpha}}{\mathrm{d}\bar{\rho}^{\alpha}} \frac{\mathrm{d}^2 \rho^{\beta}}{\left(\mathrm{d}r^{\alpha\beta}\right)^2} + \frac{\mathrm{d}U^{\beta}}{\mathrm{d}\bar{\rho}^{\beta}} \frac{\mathrm{d}^2 \rho^{\alpha}}{\left(\mathrm{d}r^{\alpha\beta}\right)^2}\right] \frac{r_i^{\alpha\beta} r_j^{\alpha\beta}}{\left(r^{\alpha\beta}\right)^2} \\
& -\left(\frac{\mathrm{d}V^{\alpha\beta}}{\mathrm{d}r^{\alpha\beta}} + \frac{\mathrm{d}U^{\alpha}}{\mathrm{d}\bar{\rho}^{\alpha}} \frac{\mathrm{d}\rho^{\beta}}{\mathrm{d}r^{\alpha\beta}} + \frac{\mathrm{d}U^{\beta}}{\mathrm{d}\bar{\rho}^{\beta}} \frac{\mathrm{d}\rho^{\alpha}}{\mathrm{d}r^{\alpha\beta}}\right) \frac{\left(r^{\alpha\beta}\right)^2 \delta_{ij} - r_i^{\alpha\beta} r_j^{\alpha\beta}}{\left(r^{\alpha\beta}\right)^3} \\
& -\frac{\mathrm{d}^2 U^{\beta}}{\left(\mathrm{d}\bar{\rho}^{\beta}\right)^2} \frac{\mathrm{d}\rho^{\alpha}}{\mathrm{d}r^{\alpha\beta}} \frac{r_i^{\alpha\beta}}{r^{\alpha\beta}} \sum_{\gamma \neq \beta} \left(\frac{\mathrm{d}\rho^{\gamma}}{\mathrm{d}r^{\gamma\beta}} \frac{r_j^{\gamma\beta}}{r^{\gamma\beta}}\right) \\
& -\frac{\mathrm{d}^2 U^{\alpha}}{\left(\mathrm{d}\bar{\rho}^{\alpha}\right)^2} \frac{\mathrm{d}\rho^{\beta}}{\mathrm{d}r^{\alpha\beta}} \frac{r_j^{\alpha\beta}}{r^{\alpha\beta}} \sum_{\gamma \neq \alpha} \left(\frac{\mathrm{d}\rho^{\gamma}}{\mathrm{d}r^{\alpha\gamma}} \frac{r_i^{\alpha\gamma}}{r^{\alpha\gamma}}\right) \\
& -\sum_{\gamma \neq \alpha, \beta} \left[\frac{\mathrm{d}^2 U^{\gamma}}{\left(\mathrm{d}\bar{\rho}^{\gamma}\right)^2} \frac{\mathrm{d}\rho^{\alpha}}{\mathrm{d}r^{\alpha\gamma}} \frac{\mathrm{d}\rho^{\beta}}{\mathrm{d}r^{\gamma\beta}} \frac{r_i^{\alpha\gamma}}{r^{\alpha\gamma}} \frac{r_j^{\gamma\beta}}{r^{\gamma\beta}}\right],
\end{aligned} \tag{12}$$

where δ is the Kronecker symbol. In the case of $\alpha = \beta$, considering all atoms are in their equilibrium positions, there should be

$$\left.\frac{\partial^2 \Psi}{\partial \mathbf{u}^{\alpha} \partial \mathbf{u}^{\alpha}}\right|_{\mathbf{x}_0} = -\sum_{\gamma \neq \alpha} \left.\frac{\partial^2 \Psi}{\partial \mathbf{u}^{\alpha} \partial \mathbf{u}^{\gamma}}\right|_{\mathbf{x}_0}, \tag{13}$$

i.e., $\mathbf{\Phi}^{\alpha\alpha}$ can be expressed by summation of the force constant matrix component with respect to atom α and its neighboring atoms.

The correlation between the force constant matrix and the deformation gradient tensor $\mathbf{F}$ can be established based on the Cauchy-Born hypothesis [8], which bridges the atomic motion with macroscopic deformation by

$$\mathbf{r}^{\alpha\beta} = \mathbf{F}\mathbf{R}^{\alpha\beta} \tag{14}$$

for simple crystal lattices, and

$$\mathbf{r}^{\alpha\beta} = \mathbf{F}\left(\mathbf{R}^{\alpha\beta} + \mathbf{Z}^{a'} - \mathbf{Z}^{a}\right) \tag{15}$$

for complex crystal lattices [10]. Here $\mathbf{R}^{\alpha\beta}$ and $\mathbf{r}^{\alpha\beta}$ denote the relative position vectors between atoms α and β in the undeformed and deformed configurations, respectively, and $\mathbf{Z}^{a}$ ($\mathbf{Z}^{a'}$) is the inner displacement of atom α (β) scaled in the undeformed configuration. According to Eqs. (12) and (14) or (15), the derivative of $\mathbf{\Phi}^{\alpha\beta}$ ($\alpha \neq \beta$) with respect $\mathbf{F}$ can be expressed as

$$
\begin{aligned}
\frac{\partial\left(\dfrac{\partial^2\Psi}{\partial u_i^\alpha \partial u_j^\beta}\right)}{\partial F_{kl}} =& -\left[\frac{\mathrm{d}^3V^{\alpha\beta}}{\left(\mathrm{d}r^{\alpha\beta}\right)^3}+\frac{\mathrm{d}U^\alpha}{\mathrm{d}\bar{\rho}^\alpha}\frac{\mathrm{d}^3\rho^\beta}{\left(\mathrm{d}r^{\alpha\beta}\right)^3}+\frac{\mathrm{d}U^\beta}{\mathrm{d}\bar{\rho}^\beta}\frac{\mathrm{d}^3\rho^\alpha}{\left(\mathrm{d}r^{\alpha\beta}\right)^3}\right]\frac{r_i^{\alpha\beta}r_j^{\alpha\beta}r_k^{\alpha\beta}r_{l'}^{\alpha\beta}F_{ll'}^{-1}}{\left(r^{\alpha\beta}\right)^3}\\
&-\frac{\mathrm{d}^2U^\alpha}{\left(\mathrm{d}\bar{\rho}^\alpha\right)^2}\frac{\mathrm{d}^2\rho^\beta}{\left(\mathrm{d}r^{\alpha\beta}\right)^2}\frac{r_i^{\alpha\beta}r_j^{\alpha\beta}}{\left(r^{\alpha\beta}\right)^2}\sum_{\gamma\neq\alpha}\left(\frac{\mathrm{d}\rho^\gamma}{\mathrm{d}r^{\alpha\gamma}}\frac{r_k^{\alpha\gamma}r_{l'}^{\alpha\gamma}F_{ll'}^{-1}}{r^{\alpha\gamma}}\right)\\
&-\frac{\mathrm{d}^2U^\beta}{\left(\mathrm{d}\bar{\rho}^\beta\right)^2}\frac{\mathrm{d}^2\rho^\alpha}{\left(\mathrm{d}r^{\alpha\beta}\right)^2}\frac{r_i^{\alpha\beta}r_j^{\alpha\beta}}{\left(r^{\alpha\beta}\right)^2}\sum_{\gamma\neq\beta}\left(\frac{\mathrm{d}\rho^\gamma}{\mathrm{d}r^{\beta\gamma}}\frac{r_k^{\beta\gamma}r_{l'}^{\beta\gamma}F_{ll'}^{-1}}{r^{\beta\gamma}}\right)\\
&-\left[\frac{\mathrm{d}^2V^{\alpha\beta}}{\left(\mathrm{d}r^{\alpha\beta}\right)^2}+\frac{\mathrm{d}U^\alpha}{\mathrm{d}\bar{\rho}^\alpha}\frac{\mathrm{d}^2\rho^\beta}{\left(\mathrm{d}r^{\alpha\beta}\right)^2}+\frac{\mathrm{d}U^\beta}{\mathrm{d}\bar{\rho}^\beta}\frac{\mathrm{d}^2\rho^\alpha}{\left(\mathrm{d}r^{\alpha\beta}\right)^2}-\frac{1}{r^{\alpha\beta}}\left(\frac{\mathrm{d}V^{\alpha\beta}}{\mathrm{d}r^{\alpha\beta}}+\frac{\mathrm{d}U^\alpha}{\mathrm{d}\bar{\rho}^\alpha}\frac{\mathrm{d}\rho^\beta}{\mathrm{d}r^{\alpha\beta}}+\frac{\mathrm{d}U^\beta}{\mathrm{d}\bar{\rho}^\beta}\frac{\mathrm{d}\rho^\alpha}{\mathrm{d}r^{\alpha\beta}}\right)\right]\\
&\times\frac{\left(r^{\alpha\beta}\right)^2\left(r_i^{\alpha\beta}\delta_{jk}+r_j^{\alpha\beta}\delta_{ik}+r_k^{\alpha\beta}\delta_{ij}\right)r_{l'}^{\alpha\beta}F_{ll'}^{-1}-3r_i^{\alpha\beta}r_j^{\alpha\beta}r_k^{\alpha\beta}r_{l'}^{\alpha\beta}F_{ll'}^{-1}}{\left(r^{\alpha\beta}\right)^4}\\
&-\frac{\mathrm{d}U^\alpha}{\mathrm{d}\bar{\rho}^\alpha}\frac{\mathrm{d}\rho^\beta}{\mathrm{d}r^{\alpha\beta}}\frac{\left(r^{\alpha\beta\delta}\right)_{ij}^2-r_i^{\alpha\beta}r_j^{\alpha\beta}}{\left(r^{\alpha\beta}\right)^3}\sum_{\gamma\neq\alpha}\left(\frac{\mathrm{d}\rho^\gamma}{\mathrm{d}r^{\alpha\gamma}}\frac{r_k^{\alpha\gamma}r_{l'}^{\alpha\gamma}F_{ll'}^{-1}}{r^{\alpha\gamma}}\right)\\
&-\frac{\mathrm{d}U^\beta}{\mathrm{d}\bar{\rho}^\beta}\frac{\mathrm{d}\rho^\alpha}{\mathrm{d}r^{\alpha\beta}}\frac{\left(r^{\alpha\beta\delta}\right)_{ij}^2-r_i^{\alpha\beta}r_j^{\alpha\beta}}{\left(r^{\alpha\beta}\right)^3}\sum_{\gamma\neq\beta}\left(\frac{\mathrm{d}\rho^\gamma}{\mathrm{d}r^{\beta\gamma}}\frac{r_k^{\beta\gamma}r_{l'}^{\beta\gamma}F_{ll'}^{-1}}{r^{\beta\gamma}}\right)\\
&-\frac{\mathrm{d}^3U^\beta}{\left(\mathrm{d}\bar{\rho}^\beta\right)^3}\frac{\mathrm{d}\rho^\alpha}{\mathrm{d}r^{\alpha\beta}}\frac{r_i^{\alpha\beta}}{r^{\alpha\beta}}\sum_{\gamma\neq\beta}\left(\frac{\mathrm{d}\rho^\gamma}{\mathrm{d}r^{\beta\gamma}}\frac{r_k^{\beta\gamma}r_{l'}^{\beta\gamma}F_{ll'}^{-1}}{r^{\beta\gamma}}\right)\sum_{\gamma\neq\beta}\left(\frac{\mathrm{d}\rho^\gamma}{\mathrm{d}r^{\gamma\beta}}\frac{r_j^{\gamma\beta}}{r^{\gamma\beta}}\right)\\
&-\frac{\mathrm{d}^3U^\alpha}{\left(\mathrm{d}\bar{\rho}^\alpha\right)^3}\frac{\mathrm{d}\rho^\beta}{\mathrm{d}r^{\alpha\beta}}\frac{r_j^{\alpha\beta}}{r^{\alpha\beta}}\sum_{\gamma\neq\alpha}\left(\frac{\mathrm{d}\rho^\gamma}{\mathrm{d}r^{\alpha\gamma}}\frac{r_k^{\alpha\gamma}r_{l'}^{\alpha\gamma}F_{ll'}^{-1}}{r^{\alpha\gamma}}\right)\sum_{\gamma\neq\alpha}\left(\frac{\mathrm{d}\rho^\gamma}{\mathrm{d}r^{\alpha\gamma}}\frac{r_i^{\alpha\gamma}}{r^{\alpha\gamma}}\right)\\
&-\frac{\mathrm{d}^2U^\beta}{\left(\mathrm{d}\bar{\rho}^\beta\right)^2}\left[\frac{\mathrm{d}^2\rho^\alpha}{\left(\mathrm{d}r^{\alpha\beta}\right)^2}r^{\alpha\beta}-\frac{\mathrm{d}\rho^\alpha}{\mathrm{d}r^{\alpha\beta}}\right]\frac{r_i^{\alpha\beta}r_k^{\alpha\beta}r_{l'}^{\alpha\beta}F_{ll'}^{-1}}{\left(r^{\alpha\beta}\right)^3}\sum_{\gamma\neq\beta}\left(\frac{\mathrm{d}\rho^\gamma}{\mathrm{d}r^{\gamma\beta}}\frac{r_j^{\gamma\beta}}{r^{\gamma\beta}}\right)\\
&-\frac{\mathrm{d}^2U^\alpha}{\left(\mathrm{d}\bar{\rho}^\alpha\right)^2}\left[\frac{\mathrm{d}^2\rho^\beta}{\left(\mathrm{d}r^{\alpha\beta}\right)^2}r^{\alpha\beta}-\frac{\mathrm{d}\rho^\beta}{\mathrm{d}r^{\alpha\beta}}\right]\frac{r_j^{\alpha\beta}r_k^{\alpha\beta}r_{l'}^{\alpha\beta}F_{ll'}^{-1}}{\left(r^{\alpha\beta}\right)^3}\sum_{\gamma\neq\alpha}\left(\frac{\mathrm{d}\rho^\gamma}{\mathrm{d}r^{\alpha\gamma}}\frac{r_i^{\alpha\gamma}}{r^{\alpha\gamma}}\right)\\
&-\frac{\mathrm{d}^2U^\beta}{\left(\mathrm{d}\bar{\rho}^\beta\right)^2}\frac{\mathrm{d}\rho^\alpha}{\mathrm{d}r^{\alpha\beta}}\frac{r_i^{\alpha\beta}}{r^{\alpha\beta}}\sum_{\gamma\neq\beta}\left[\left(\frac{\mathrm{d}^2\rho^\gamma}{\left(\mathrm{d}r^{\gamma\beta}\right)^2}r^{\gamma\beta}-\frac{\mathrm{d}\rho^\gamma}{\mathrm{d}r^{\gamma\beta}}\right)\frac{r_j^{\gamma\beta}r_k^{\gamma\beta}r_{l'}^{\gamma\beta}F_{ll'}^{-1}}{\left(r^{\gamma\beta}\right)^3}\right]\\
&-\frac{\mathrm{d}^2U^\alpha}{\left(\mathrm{d}\bar{\rho}^\alpha\right)^2}\frac{\mathrm{d}\rho^\beta}{\mathrm{d}r^{\alpha\beta}}\frac{r_j^{\alpha\beta}}{r^{\alpha\beta}}\sum_{\gamma\neq\alpha}\left[\left(\frac{\mathrm{d}^2\rho^\gamma}{\left(\mathrm{d}r^{\alpha\gamma}\right)^2}r^{\alpha\gamma}-\frac{\mathrm{d}\rho^\gamma}{\mathrm{d}r^{\alpha\gamma}}\right)\frac{r_i^{\alpha\gamma}r_k^{\alpha\gamma}r_{l'}^{\alpha\gamma}F_{ll'}^{-1}}{\left(r^{\alpha\gamma}\right)^3}\right]\\
&-\frac{\mathrm{d}^2U^\beta}{\left(\mathrm{d}\bar{\rho}^\beta\right)^2}\frac{\mathrm{d}\rho^\alpha}{\mathrm{d}r^{\alpha\beta}}\frac{\delta_{ik}r_{l'}^{\alpha\beta}F_{ll'}^{-1}}{r^{\alpha\beta}}\sum_{\gamma\neq\beta}\left(\frac{\mathrm{d}\rho^\gamma}{\mathrm{d}r^{\gamma\beta}}\frac{r_j^{\gamma\beta}}{r^{\gamma\beta}}\right)-\frac{\mathrm{d}^2U^\alpha}{\left(\mathrm{d}\bar{\rho}^\alpha\right)^2}\frac{\mathrm{d}\rho^\beta}{\mathrm{d}r^{\alpha\beta}}\frac{\delta_{jk}r_{l'}^{\alpha\beta}F_{ll'}^{-1}}{r^{\alpha\beta}}\sum_{\gamma\neq\alpha}\left(\frac{\mathrm{d}\rho^\gamma}{\mathrm{d}r^{\alpha\gamma}}\frac{r_i^{\alpha\gamma}}{r^{\alpha\gamma}}\right)\\
&-\frac{\mathrm{d}^2U^\beta}{\left(\mathrm{d}\bar{\rho}^\beta\right)^2}\frac{\mathrm{d}\rho^\alpha}{\mathrm{d}r^{\alpha\beta}}\frac{r_i^{\alpha\beta}}{r^{\alpha\beta}}\sum_{\gamma\neq\beta}\left(\frac{\mathrm{d}\rho^\gamma}{\mathrm{d}r^{\gamma\beta}}\frac{\delta_{jk}r_{l'}^{\gamma\beta}F_{ll'}^{-1}}{r^{\gamma\beta}}\right)-\frac{\mathrm{d}^2U^\alpha}{\left(\mathrm{d}\bar{\rho}^\alpha\right)^2}\frac{\mathrm{d}\rho^\beta}{\mathrm{d}r^{\alpha\beta}}\frac{r_j^{\alpha\beta}}{r^{\alpha\beta}}\sum_{\gamma\neq\alpha}\left(\frac{\mathrm{d}\rho^\gamma}{\mathrm{d}r^{\alpha\gamma}}\frac{\delta_{ik}r_{l'}^{\alpha\gamma}F_{ll'}^{-1}}{r^{\alpha\gamma}}\right)\\
&-\sum_{\gamma\neq\alpha,\beta}\left[\frac{\mathrm{d}^3U^\gamma}{\left(\mathrm{d}\bar{\rho}^\gamma\right)^3}\frac{\mathrm{d}\rho^\alpha}{\mathrm{d}r^{\alpha\gamma}}\frac{\mathrm{d}\rho^\beta}{\mathrm{d}r^{\gamma\beta}}\frac{r_i^{\alpha\gamma}}{r^{\alpha\gamma}}\frac{r_j^{\gamma\beta}}{r^{\gamma\beta}}\sum_{\eta\neq\gamma}\left(\frac{\mathrm{d}\rho^\eta}{\mathrm{d}r^{\eta\gamma}}\frac{r_k^{\eta\gamma}r_{l'}^{\eta\gamma}F_{ll'}^{-1}}{r^{\eta\gamma}}\right)\right]\\
&-\sum_{\gamma\neq\alpha,\beta}\left[\frac{\mathrm{d}^2U^\gamma}{\left(\mathrm{d}\bar{\rho}^\gamma\right)^2}\frac{\mathrm{d}\rho^\beta}{\mathrm{d}r^{\gamma\beta}}\left(\frac{\mathrm{d}^2\rho^\alpha}{\left(\mathrm{d}r^{\alpha\gamma}\right)^2}r^{\alpha\gamma}-\frac{\mathrm{d}\rho^\alpha}{\mathrm{d}r^{\alpha\gamma}}\right)\frac{r_i^{\alpha\gamma}r_j^{\gamma\beta}r_k^{\alpha\gamma}r_{l'}^{\alpha\gamma}F_{ll'}^{-1}}{\left(r^{\alpha\gamma}\right)^3r^{\gamma\beta}}\right]\\
&-\sum_{\gamma\neq\alpha,\beta}\left[\frac{\mathrm{d}^2U^\gamma}{\left(\mathrm{d}\bar{\rho}^\gamma\right)^2}\frac{\mathrm{d}\rho^\alpha}{\mathrm{d}r^{\alpha\gamma}}\left(\frac{\mathrm{d}^2\rho^\beta}{\left(\mathrm{d}r^{\gamma\beta}\right)^2}r^{\gamma\beta}-\frac{\mathrm{d}\rho^\beta}{\mathrm{d}r^{\gamma\beta}}\right)\frac{r_i^{\alpha\gamma}r_j^{\gamma\beta}r_k^{\gamma\beta}r_{l'}^{\gamma\beta}F_{ll'}^{-1}}{\left(r^{\gamma\beta}\right)^3r^{\alpha\gamma}}\right]\\
&-\sum_{\gamma\neq\alpha,\beta}\left[\frac{\mathrm{d}^2U^\gamma}{\left(\mathrm{d}\bar{\rho}^\gamma\right)^2}\frac{\mathrm{d}\rho^\alpha}{\mathrm{d}r^{\alpha\gamma}}\frac{\mathrm{d}\rho^\beta}{\mathrm{d}r^{\gamma\beta}}\frac{\delta_{jk}r_i^{\alpha\gamma}r_{l'}^{\alpha\gamma}F_{ll'}^{-1}+\delta_{ik}r_j^{\gamma\beta}r_{l'}^{\gamma\beta}F_{ll'}^{-1}}{r^{\alpha\gamma}r^{\gamma\beta}}\right].
\end{aligned}
\tag{16}
$$

III. RESPONSE OF THE POTENTIAL ENERGY CHANGE TO THE PHONON DISPLACEMENT IN SIMPLE CRYSTAL LATTICES

Consider a crystal supercell under periodical boundary conditions (PBC) with N primitive cells, each of which contains n basis atoms. The displacements of each atom can be viewed as superposition of the oscillation for all the lattice waves [7]:

$$\mathbf{u}\begin{pmatrix}A\\a\end{pmatrix}=\frac{1}{\sqrt{Nm_a}}\sum_{k,j}^{N,3n}\mathbf{e}\left(a\left|\begin{matrix}\mathbf{k}\\j\end{matrix}\right.\right)Q\begin{pmatrix}\mathbf{k}\\j\end{pmatrix}e^{i\mathbf{k}\cdot\mathbf{X}(A)}, \tag{17}$$

where $\mathbf{e}\left(a\left|\begin{smallmatrix}\mathbf{k}\\j\end{smallmatrix}\right.\right)$ is the ath component of the jth normalized eigenvector of $\mathbf{D}^{\mathbf{k}}$ whose component is given in Eq. (3), and $Q\left(\begin{smallmatrix}\mathbf{k}\\j\end{smallmatrix}\right)$ is the jth normal coordinate with respect to $\mathbf{k}$. Then the total potential change as a function of atomic displacements near the equilibrium positions $\mathbf{x}_0$ can be expanded as

$$\begin{aligned}\Delta\Psi=\sum_{s=2}^{\infty}\Delta\Psi_s=&\sum_{s=2}^{\infty}\frac{1}{s!}\frac{1}{N^{(s-2)/2}}\sum_{k,j}^{N,3n}\sum_{k',j'}^{N,3n}\cdots\sum_{k^{(s-1)},j^{(s-1)}}^{N,3n}\Theta\left(\mathbf{k}+\mathbf{k}'+\cdots+\mathbf{k}^{(s-1)}\right)\\&Q\begin{pmatrix}\mathbf{k}\\j\end{pmatrix}Q\begin{pmatrix}\mathbf{k}'\\j'\end{pmatrix}\cdots Q\begin{pmatrix}\mathbf{k}^{(s-1)}\\j^{(s-1)}\end{pmatrix}\tilde{\Phi}\begin{pmatrix}\mathbf{k}&\mathbf{k}'&\cdots&\mathbf{k}^{(s-1)}\\j&j'&\cdots&j^{(s-1)}\end{pmatrix}.\end{aligned} \tag{18}$$

Here, the Θ function is defined as

$$\Theta(\mathbf{k})=\frac{1}{N}\sum_{A}^{N}e^{i\mathbf{k}\cdot\mathbf{X}(A)}, \tag{19}$$

and

$$\begin{aligned}\tilde{\Phi}\begin{pmatrix}\mathbf{k}&\mathbf{k}'&\cdots&\mathbf{k}^{(s-1)}\\j&j'&\cdots&j^{(s-1)}\end{pmatrix}=&\sum_{a}^{n}\sum_{A',a'}^{\infty,n}\cdots\sum_{A^{(s-1)},a^{(s-1)}}^{\infty,n}\frac{1}{\sqrt{m_am_{a'}\cdots m_{a^{(s-1)}}}}\mathbf{\Phi}\begin{pmatrix}\mathbf{k}&\mathbf{k}'&\cdots&\mathbf{k}^{(s-1)}\\j&j'&\cdots&j^{(s-1)}\end{pmatrix}\\&\cdot\mathbf{e}\left(a\left|\begin{matrix}\mathbf{k}\\j\end{matrix}\right.\right)\cdot\mathbf{e}\left(a'\left|\begin{matrix}\mathbf{k}'\\j'\end{matrix}\right.\right)\cdot\cdots\cdot\mathbf{e}\left(a^{(s-1)}\left|\begin{matrix}\mathbf{k}^{(s-1)}\\j^{(s-1)}\end{matrix}\right.\right)e^{i\left[\mathbf{k}'\cdot\mathbf{X}(A')+\cdots+\mathbf{k}^{(s-1)}\cdot\mathbf{X}(A^{(s-1)})\right]},\end{aligned} \tag{20}$$

where the force constant tensor $\mathbf{\Phi}$ is given by

$$\mathbf{\Phi}\begin{pmatrix}\mathbf{k}&\mathbf{k}'&\cdots&\mathbf{k}^{(s-1)}\\j&j'&\cdots&j^{(s-1)}\end{pmatrix}=\left.\frac{\partial^s\Psi}{\partial\mathbf{u}\begin{pmatrix}A\\a\end{pmatrix}\partial\mathbf{u}\begin{pmatrix}A'\\a'\end{pmatrix}\cdots\partial\mathbf{u}\begin{pmatrix}A^{(s-1)}\\a^{(s-1)}\end{pmatrix}}\right|_{\mathbf{x}_0}. \tag{21}$$

Particularly, the second-order term in Eq. (18) can be simplified as

$$\Delta\Psi_2=\frac{1}{2}\sum_{k,j}^{N,3n}\omega^2\begin{pmatrix}\mathbf{k}\\j\end{pmatrix}\left|Q\begin{pmatrix}\mathbf{k}\\j\end{pmatrix}\right|^2, \tag{22}$$

where $\omega^2\left(\begin{smallmatrix}\mathbf{k}\\j\end{smallmatrix}\right)$ is the jth eigenvalue of $\mathbf{D}^{\mathbf{k}}$.

Let us consider the case only the $\left(\begin{smallmatrix}\hat{\mathbf{k}}\\\hat{j}\end{smallmatrix}\right)$ phonon is excited in a simple crystal lattice ($n=1$, so the index a can be omitted). In this case, all the normal coordinates but $Q\left(\begin{smallmatrix}\hat{\mathbf{k}}\\\hat{j}\end{smallmatrix}\right)$ and $Q\left(\begin{smallmatrix}-\hat{\mathbf{k}}\\\hat{j}\end{smallmatrix}\right)$ vanish, and $\mathbf{e}\left(\begin{smallmatrix}\hat{\mathbf{k}}\\\hat{j}\end{smallmatrix}\right)$ and $\mathbf{e}\left(\begin{smallmatrix}-\hat{\mathbf{k}}\\\hat{j}\end{smallmatrix}\right)$ become the same real vector as $\mathbf{D}^{\mathbf{k}}$ degenerates to a real matrix. We will show that the sth-order term in Eq. (18) with respect to the phonon displacement u_A of the excited lattice wave can be expressed as $\Delta\Psi_s=c_s\left|u_A\right|^s$, in which $\Delta\Psi_s$ as well as the coefficients c_s (only $s\leqslant 4$ considered here) can be simplified into different expressions for different types of $\hat{\mathbf{k}}$ as follows:

• If $\hat{\mathbf{k}}=\mathbf{b}_r/2$, where $\mathbf{b}_r$ is a reciprocal lattice vector (i.e., $\mathbf{b}_r=\sum_{i=1}^{3}n_i\mathbf{b}_i$, in which n_i is an integer and $\mathbf{b}_i$ is the ith reciprocal basis vector), the $\hat{\mathbf{k}}$ point in on the zone boundary, and it has

$$\hat{\mathbf{k}}\cdot\mathbf{X}(A)=l\pi, \tag{23}$$

where l is an integer. In this case, $\hat{\mathbf{k}}$ and $-\hat{\mathbf{k}}$ are equivalent wave vectors, and $Q\begin{pmatrix}\hat{\mathbf{k}}\\ \hat{j}\end{pmatrix}$ and $Q\begin{pmatrix}-\hat{\mathbf{k}}\\ \hat{j}\end{pmatrix}$ are also equivalent, which degenerate to the same real number. Then Eq. (17) can be simplified as

$$\mathbf{u}(A)=\frac{1}{\sqrt{Nm}}\mathbf{e}\begin{pmatrix}\hat{\mathbf{k}}\\ \hat{j}\end{pmatrix}Q\begin{pmatrix}\hat{\mathbf{k}}\\ \hat{j}\end{pmatrix}\cos\left(\hat{\mathbf{k}}\cdot\mathbf{X}(A)\right). \tag{24}$$

Compared with an excited lattice wave $\mathbf{u}(A)=\mathbf{w}\cos\left(\hat{\mathbf{k}}\cdot\mathbf{X}(A)+\varphi\right)$ and considering Eq. (23), it has

$$\left|Q\begin{pmatrix}\hat{\mathbf{k}}\\ \hat{j}\end{pmatrix}\right|=w\sqrt{Nm}, \tag{25}$$

in which the wave amplitude w is re-defined as $|\mathbf{w}||\cos\varphi|$. Substituting Eq. (25) into Eq. (22), Eqs. (23) and (25) into Eq. (18), we have

$$\Delta\Psi_2=\frac{1}{2}Nm\omega^2\begin{pmatrix}\hat{\mathbf{k}}\\ \hat{j}\end{pmatrix}w^2, \tag{26}$$

$$\Delta\Psi_3=0, \tag{27}$$

$$\begin{aligned}\Delta\Psi_4&=\frac{1}{24N}Q\begin{pmatrix}\hat{\mathbf{k}}\\ \hat{j}\end{pmatrix}Q\begin{pmatrix}\hat{\mathbf{k}}\\ \hat{j}\end{pmatrix}Q\begin{pmatrix}\hat{\mathbf{k}}\\ \hat{j}\end{pmatrix}Q\begin{pmatrix}\hat{\mathbf{k}}\\ \hat{j}\end{pmatrix}\tilde{\Phi}\begin{pmatrix}\hat{\mathbf{k}} & \hat{\mathbf{k}} & \hat{\mathbf{k}} & \hat{\mathbf{k}}\\ \hat{j} & \hat{j} & \hat{j} & \hat{j}\end{pmatrix}\\&=\frac{Nw^4}{24}\left[\sum_{A'}^{\infty}\sum_{A''}^{\infty}\sum_{A'''}^{\infty}\mathbf{\Phi}\begin{pmatrix}0 & A' & A'' & A'''\end{pmatrix}\cos\left(\hat{k}\cdot(\mathbf{X}(A')+\mathbf{X}(A'')+\mathbf{X}(A'''))\right)\right]\\&\quad\cdot\mathbf{e}\begin{pmatrix}\hat{\mathbf{k}}\\ \hat{j}\end{pmatrix}\cdot\mathbf{e}\begin{pmatrix}\hat{\mathbf{k}}\\ \hat{j}\end{pmatrix}\cdot\mathbf{e}\begin{pmatrix}\hat{\mathbf{k}}\\ \hat{j}\end{pmatrix}\cdot\mathbf{e}\begin{pmatrix}\hat{\mathbf{k}}\\ \hat{j}\end{pmatrix}.\end{aligned} \tag{28}$$

- If $\hat{\mathbf{k}}=\mathbf{b}_r/3$, $\hat{\mathbf{k}}$ and $-\hat{\mathbf{k}}$ are no longer equivalent, and it has

$$\begin{aligned}\mathbf{u}(A)&=\frac{1}{\sqrt{Nm}}\left[\mathbf{e}\begin{pmatrix}\hat{\mathbf{k}}\\ \hat{j}\end{pmatrix}Q\begin{pmatrix}\hat{\mathbf{k}}\\ \hat{j}\end{pmatrix}e^{i\hat{\mathbf{k}}\cdot\mathbf{X}(A)}+\mathbf{e}\begin{pmatrix}-\hat{\mathbf{k}}\\ \hat{j}\end{pmatrix}Q\begin{pmatrix}-\hat{\mathbf{k}}\\ \hat{j}\end{pmatrix}e^{-i\hat{\mathbf{k}}\cdot\mathbf{X}(A)}\right]\\&=\frac{2}{\sqrt{Nm}}\mathbf{e}\begin{pmatrix}\hat{\mathbf{k}}\\ \hat{j}\end{pmatrix}\left|Q\begin{pmatrix}\hat{\mathbf{k}}\\ \hat{j}\end{pmatrix}\right|\cos\left[\hat{\mathbf{k}}\cdot\mathbf{X}(A)+\varphi_Q\begin{pmatrix}\hat{\mathbf{k}}\\ \hat{j}\end{pmatrix}\right],\end{aligned} \tag{29}$$

where $\varphi_Q\begin{pmatrix}\hat{\mathbf{k}}\\ \hat{j}\end{pmatrix}$ is the phase of $Q\begin{pmatrix}\hat{\mathbf{k}}\\ \hat{j}\end{pmatrix}$. Compared with an exited lattice wave $\mathbf{u}(A)=\mathbf{w}\cos\left(\hat{\mathbf{k}}\cdot\mathbf{X}(A)+\varphi\right)$, it has

$$\left|Q\begin{pmatrix}\hat{\mathbf{k}}\\ \hat{j}\end{pmatrix}\right|=\frac{1}{2}w\sqrt{Nm}, \tag{30}$$

$$\varphi_Q\begin{pmatrix}\hat{\mathbf{k}}\\ \hat{j}\end{pmatrix}=\varphi, \tag{31}$$

in which $w=|\mathbf{w}|$. Substituting Eq. (30) into Eq. (22), Eqs. (30) and (31) into Eq. (18), we can get

$$\Delta\Psi_2=\frac{1}{4}Nm\omega^2\begin{pmatrix}\hat{\mathbf{k}}\\ \hat{j}\end{pmatrix}w^2, \tag{32}$$

$$\begin{aligned}\Delta\Psi_3&=\frac{1}{6\sqrt{N}}\left[Q\begin{pmatrix}\hat{\mathbf{k}}\\ \hat{j}\end{pmatrix}Q\begin{pmatrix}\hat{\mathbf{k}}\\ \hat{j}\end{pmatrix}Q\begin{pmatrix}\hat{\mathbf{k}}\\ \hat{j}\end{pmatrix}\tilde{\Phi}\begin{pmatrix}\hat{\mathbf{k}} & \hat{\mathbf{k}} & \hat{\mathbf{k}}\\ \hat{j} & \hat{j} & \hat{j}\end{pmatrix}+Q\begin{pmatrix}-\hat{\mathbf{k}}\\ \hat{j}\end{pmatrix}Q\begin{pmatrix}-\hat{\mathbf{k}}\\ \hat{j}\end{pmatrix}Q\begin{pmatrix}-\hat{\mathbf{k}}\\ \hat{j}\end{pmatrix}\tilde{\Phi}\begin{pmatrix}-\hat{\mathbf{k}} & -\hat{\mathbf{k}} & -\hat{\mathbf{k}}\\ \hat{j} & \hat{j} & \hat{j}\end{pmatrix}\right]\\&=\frac{Nw^3}{24}\left[\sum_{A'}^{\infty}\sum_{A''}^{\infty}\mathbf{\Phi}\begin{pmatrix}0 & A' & A''\end{pmatrix}\cos\left(\hat{k}\cdot(\mathbf{X}(A')+\mathbf{X}(A''))+3\varphi\right)\right]\cdot\mathbf{e}\begin{pmatrix}\hat{\mathbf{k}}\\ \hat{j}\end{pmatrix}\cdot\mathbf{e}\begin{pmatrix}\hat{\mathbf{k}}\\ \hat{j}\end{pmatrix}\cdot\mathbf{e}\begin{pmatrix}\hat{\mathbf{k}}\\ \hat{j}\end{pmatrix},\end{aligned} \tag{33}$$

$$\begin{aligned}\Delta\Psi_4&=\frac{6}{24N}Q\begin{pmatrix}\hat{\mathbf{k}}\\ \hat{j}\end{pmatrix}Q\begin{pmatrix}\hat{\mathbf{k}}\\ \hat{j}\end{pmatrix}Q\begin{pmatrix}-\hat{\mathbf{k}}\\ \hat{j}\end{pmatrix}Q\begin{pmatrix}-\hat{\mathbf{k}}\\ \hat{j}\end{pmatrix}\tilde{\Phi}\begin{pmatrix}\hat{\mathbf{k}} & \hat{\mathbf{k}} & -\hat{\mathbf{k}} & -\hat{\mathbf{k}}\\ \hat{j} & \hat{j} & \hat{j} & \hat{j}\end{pmatrix}\\&=\frac{Nw^4}{64}\left[\sum_{A'}^{\infty}\sum_{A''}^{\infty}\sum_{A'''}^{\infty}\mathbf{\Phi}\begin{pmatrix}0 & A' & A'' & A'''\end{pmatrix}\cos\left(\hat{k}\cdot(\mathbf{X}(A')-\mathbf{X}(A'')-\mathbf{X}(A'''))\right)\right]\\&\quad\cdot\mathbf{e}\begin{pmatrix}\hat{\mathbf{k}}\\ \hat{j}\end{pmatrix}\cdot\mathbf{e}\begin{pmatrix}\hat{\mathbf{k}}\\ \hat{j}\end{pmatrix}\cdot\mathbf{e}\begin{pmatrix}\hat{\mathbf{k}}\\ \hat{j}\end{pmatrix}\cdot\mathbf{e}\begin{pmatrix}\hat{\mathbf{k}}\\ \hat{j}\end{pmatrix}.\end{aligned} \tag{34}$$

• If $\hat{\mathbf{k}} = \mathbf{b}_r/4$, Eqs. (27) and (32) still work. Besides, we have

$$\begin{aligned}\Delta\Psi_4 = \frac{1}{24N}\Bigg[&Q\begin{pmatrix}\hat{\mathbf{k}}\\ \hat{j}\end{pmatrix}Q\begin{pmatrix}\hat{\mathbf{k}}\\ \hat{j}\end{pmatrix}Q\begin{pmatrix}\hat{\mathbf{k}}\\ \hat{j}\end{pmatrix}Q\begin{pmatrix}\hat{\mathbf{k}}\\ \hat{j}\end{pmatrix}\tilde{\Phi}\begin{pmatrix}\hat{\mathbf{k}} & \hat{\mathbf{k}} & \hat{\mathbf{k}} & \hat{\mathbf{k}}\\ \hat{j} & \hat{j} & \hat{j} & \hat{j}\end{pmatrix}\\ &+Q\begin{pmatrix}-\hat{\mathbf{k}}\\ \hat{j}\end{pmatrix}Q\begin{pmatrix}-\hat{\mathbf{k}}\\ \hat{j}\end{pmatrix}Q\begin{pmatrix}-\hat{\mathbf{k}}\\ \hat{j}\end{pmatrix}Q\begin{pmatrix}-\hat{\mathbf{k}}\\ \hat{j}\end{pmatrix}\tilde{\Phi}\begin{pmatrix}-\hat{\mathbf{k}} & -\hat{\mathbf{k}} & -\hat{\mathbf{k}} & -\hat{\mathbf{k}}\\ \hat{j} & \hat{j} & \hat{j} & \hat{j}\end{pmatrix}\\ &+6Q\begin{pmatrix}\hat{\mathbf{k}}\\ \hat{j}\end{pmatrix}Q\begin{pmatrix}\hat{\mathbf{k}}\\ \hat{j}\end{pmatrix}Q\begin{pmatrix}-\hat{\mathbf{k}}\\ \hat{j}\end{pmatrix}Q\begin{pmatrix}-\hat{\mathbf{k}}\\ \hat{j}\end{pmatrix}\tilde{\Phi}\begin{pmatrix}\hat{\mathbf{k}} & \hat{\mathbf{k}} & -\hat{\mathbf{k}} & -\hat{\mathbf{k}}\\ \hat{j} & \hat{j} & \hat{j} & \hat{j}\end{pmatrix}\Bigg]\\ =\frac{Nw^4}{192}\Bigg\{&\sum_{A'}^{\infty}\sum_{A''}^{\infty}\sum_{A'''}^{\infty}\mathbf{\Phi}\begin{pmatrix}0 & A' & A'' & A'''\end{pmatrix}\Big[\cos\Big(\hat{k}\cdot(\mathbf{X}(A')+\mathbf{X}(A'')+\mathbf{X}(A'''))+4\varphi\Big)\\ &+3\cos\Big(\hat{k}\cdot(\mathbf{X}(A')-\mathbf{X}(A'')-\mathbf{X}(A'''))\Big)\Big]\Bigg\}\cdot\mathbf{e}\begin{pmatrix}\hat{\mathbf{k}}\\ \hat{j}\end{pmatrix}\cdot\mathbf{e}\begin{pmatrix}\hat{\mathbf{k}}\\ \hat{j}\end{pmatrix}\cdot\mathbf{e}\begin{pmatrix}\hat{\mathbf{k}}\\ \hat{j}\end{pmatrix}\cdot\mathbf{e}\begin{pmatrix}\hat{\mathbf{k}}\\ \hat{j}\end{pmatrix}.\end{aligned} \tag{35}$$

• For other cases of $\hat{\mathbf{k}}$, Eqs. (27), (32) and (34) still work.

In summary, if only the $\begin{pmatrix}\hat{\mathbf{k}}\\ \hat{j}\end{pmatrix}$ phonon is excited in a simple lattice, considering $w = |u_A|$, $\Delta\Psi$ can be expressed as

$$\Delta\Psi = \begin{cases} c_2u_A^2 + c_3\left|u_A^3\right| + o\left(u_A^3\right) & \text{for } \hat{\mathbf{k}} = \mathbf{b}_r/3\\ c_2u_A^2 + c_4u_A^4 + o\left(u_A^4\right) & \text{for other } \hat{\mathbf{k}}.\end{cases} \tag{36}$$

In the case of $c_2 < 0$, i.e., the $\begin{pmatrix}\hat{\mathbf{k}}\\ \hat{j}\end{pmatrix}$ phonon softens, and c_3 or $c_4 > 0$, $\Delta\Psi$ exhibits a double-well profile for all types of $\hat{\mathbf{k}}$ if neglecting higher-order terms.

IV. COMPARISON OF THE DYNAMICAL EVOLUTIONS OF SOFT Γ PHONONS AND SOFT SHORT-WAVE PHONONS

It is illuminating to compare the dynamical evolutions of soft Γ phonons and soft short-wave phonons. As demonstrated in the main text, an unstable short wave could be arrested by a double-well potential in the initial stage due to the anharmonic Landau polynomial. However, as shown in Ref. [11], this phenomenon does not occur for an unstable elastic wave. In order to figure out the origin of this difference, we use an analytical scaling theory to investigate the Helmholtz free energy change ΔF as a function of the phonon displacement u_A of a perturbational elastic wave within the finite deformation framework.

Based on the finite deformation theory [12], the Helmholtz free energy F of a representative volume element (RVE) at state Y can be expanded at state X as

$$\begin{aligned}F(Y) = F(X) + \Omega(X)\Bigg[&S_{ij}(X)E_{ij} + \frac{1}{2}C^{(2)}_{ijkl}(X)E_{ij}E_{kl} + \frac{1}{6}C^{(3)}_{ijklmn}(X)E_{ij}E_{kl}E_{mn}\\ &+\frac{1}{24}C^{(4)}_{ijklmnpq}(X)E_{ij}E_{kl}E_{mn}E_{pq} + o\left(E^4\right)\Bigg],\end{aligned} \tag{37}$$

where Ω is the RVE's volume; $\mathbf{S}$ is the second Piola-Kichhoff stress tensor; $\mathbf{C}^{(2)}$, $\mathbf{C}^{(3)}$ and $\mathbf{C}^{(4)}$ are the second-, third- and fourth-order isothermal elastic constant tensors, respectively; $\mathbf{E}$ is the Lagrangian strain tensor of state Y with respect to X, defined as

$$E_{ij} = \frac{1}{2}\left(u_{i,j} + u_{j,i} + u_{r,i}u_{r,j}\right), \tag{38}$$

in which $\mathbf{u}$ is the displacement vector between state Y and X. For a system with a varied strain field, the total free energy change can be calculated by sum of those in individual RVEs,

$$\begin{aligned}\Delta F = S_{ij}\int_\Omega E_{ij}\mathrm{d}\mathbf{x} + \frac{1}{2}C^{(2)}_{ijkl}\int_\Omega E_{ij}E_{kl}\mathrm{d}\mathbf{x} + \frac{1}{6}C^{(3)}_{ijklmn}\int_\Omega E_{ij}E_{kl}E_{mn}\mathrm{d}\mathbf{x}\\ + \frac{1}{24}C^{(4)}_{ijklmnpq}\int_\Omega E_{ij}E_{kl}E_{mn}E_{pq}\mathrm{d}\mathbf{x} + o\left(E^4\right).\end{aligned} \tag{39}$$

By substituting Eq. (38) into Eq. (39), we have

$$\begin{aligned}\Delta F = \sigma_{ij}\int_\Omega u_{i,j}\mathrm{d}\mathbf{x} + \frac{1}{2}\left(C^{(2)}_{ijkl}+\sigma_{jl}\delta_{ik}\right)\int_\Omega u_{i,j}u_{k,l}\mathrm{d}\mathbf{x} + \left(\frac{1}{6}C^{(3)}_{ijklmn}+\frac{1}{2}C^{(2)}_{ijln}\delta_{km}\right)\int_\Omega u_{i,j}u_{k,l}u_{m,n}\mathrm{d}\mathbf{x} \\ + \left(\frac{1}{24}C^{(4)}_{ijklmnpq}+\frac{1}{4}C^{(3)}_{jqklmn}\delta_{ip}+\frac{1}{8}C^{(2)}_{jlnq}\delta_{ik}\delta_{mp}\right)\int_\Omega u_{i,j}u_{k,l}u_{m,n}u_{p,q}\mathrm{d}\mathbf{x} + o\left(u^4\right),\end{aligned} \tag{40}$$

where $\boldsymbol{\sigma}$ is the Cauchy stress tensor, which is equivalent to $\mathbf{S}$ if both referenced at state X.

Now consider a perturbational long elastic wave

$$\mathbf{u}(\mathbf{x}) = \mathbf{w}\sin\left(\mathbf{k}\cdot\mathbf{x}+\varphi\right) \tag{41}$$

injected into a homogenously strained supercell, where φ is the phase, $\mathbf{w}$ is the polarization vector, $\mathbf{k}$ is the wave vector perpendicular to the supercell's basal plane, and the wavelength $\lambda = 2\pi/k$ equals to the supercell's height. Substituting Eq. (41) into (40) and neglecting higher-order (>4) terms, we can get

$$\begin{aligned}\Delta F &= \frac{\Omega}{\frac{2\pi}{k}}\left[\sigma_{ij}w_ik_j\int_0^{\frac{2\pi}{k}}\cos(kx+\varphi)\mathrm{d}x + \frac{1}{2}\left(C^{(2)}_{ijkl}+\sigma_{jl}\delta_{ik}\right)w_iw_kk_jk_l\int_0^{\frac{2\pi}{k}}\cos^2(kx+\varphi)\mathrm{d}x\right. \\ &\quad + \left(\frac{1}{6}C^{(3)}_{ijklmn}+\frac{1}{2}C^{(2)}_{ijln}\delta_{km}\right)w_iw_kw_mk_jk_lk_n\int_0^{\frac{2\pi}{k}}\cos^3(kx+\varphi)\mathrm{d}x \\ &\quad \left. + \left(\frac{1}{24}C^{(4)}_{ijklmnpq}+\frac{1}{4}C^{(3)}_{jqklmn}\delta_{ip}+\frac{1}{8}C^{(2)}_{jlnq}\delta_{ik}\delta_{mp}\right)w_iw_kw_mw_pk_jk_lk_nk_q\int_0^{\frac{2\pi}{k}}\cos^4(kx+\varphi)\mathrm{d}x\right] \\ &= \frac{1}{4}\Omega k^2w^2\left(C^{(2)}_{ijkl}\bar{w}_i\bar{w}_k+\sigma_{jl}\right)\bar{k}_j\bar{k}_l + \frac{1}{64}\Omega k^4w^4\left(C^{(4)}_{ijklmnpq}\bar{w}_i\bar{w}_k\bar{w}_m\bar{w}_p + 6C^{(3)}_{jqklmn}\bar{w}_k\bar{w}_m + 3C^{(2)}_{jlnq}\right)\bar{k}_j\bar{k}_l\bar{k}_n\bar{k}_q,\end{aligned} \tag{42}$$

where $\bar{\mathbf{w}}$ and $\bar{\mathbf{k}}$ are the normalized polarization vector and wave vector, respectively. Let

$$\Lambda = \left(C^{(2)}_{ijkl}\bar{w}_i\bar{w}_k+\sigma_{jl}\right)\bar{k}_j\bar{k}_l, \tag{43}$$

$$\tilde{\Lambda} = \left(C^{(4)}_{ijklmnpq}\bar{w}_i\bar{w}_k\bar{w}_m\bar{w}_p + 6C^{(3)}_{jqklmn}\bar{w}_k\bar{w}_m + 3C^{(2)}_{jlnq}\right)\bar{k}_j\bar{k}_l\bar{k}_n\bar{k}_q, \tag{44}$$

Eq. (42) can be rewritten as

$$\Delta F = \frac{1}{4}\Omega\Lambda k^2w^2 + \frac{1}{64}\Omega\tilde{\Lambda}k^4w^4, \tag{45}$$

or

$$\Delta F = \frac{1}{4}\Omega\Lambda k^2u_A^2 + \frac{1}{64}\Omega\tilde{\Lambda}k^4u_A^4, \tag{46}$$

considering $w = |u_A|$.

According to the Λ criterion [3], an unstable elastic wave satisfies $\Lambda < 0$. Let us suppose $\tilde{\Lambda} > 0$. In this case, Eq. (46) also represents a double-well free energy, with a distance of $\sqrt{-8\Lambda/\tilde{\Lambda}}\Big/k$ from the well bottom to the center. However, as a result of $k \to 0$ for an elastic wave, this distance could be very considerable. Consequently, wave-profile distortion shown in Ref. [11], resulting from the effects of the non-linear terms in the Hamiltonian, would probably occur before the wave amplitude reaches the well bottom, i.e., being arrested by a double-well free energy, though, theoretically, the possibility of the latter cannot be completely excluded. In contrast, for an unstable short wave, the second- and the fourth-order terms in the potential could be comparable even though the amplitude is very small, which is favorable for suppressing the amplitude growth and arresting the short wave by a double-well potential in the initial stage. In general, the distinction in contribution of the anharmonic terms to the changes of potential energy and free energy essentially accounts for the different dynamical evolutions between soft short-wave phonons and soft Γ phonons.

V. DISLOCATION NUCLEATION INDUCED BY ZONE-BOUNDARY PHONON INSTABILITY IN A PERFECT CU CRYSTAL UNDER SIMPLE SHEAR

In this section, we will demonstrate how a Shockley partial dislocation is nucleated induced by zone-boundary phonon instability in a perfect Cu crystal under $[11\bar{2}](111)$ simple shear, and verify the generality of our proposed mechanism in the main text for description of how soft phonons turn into lattice defects.

Firstly, we employ *Phorion* to predict the critical engineering shear strain ε^* and the lattice instability mode. Based on the Mishin EAM potential of Cu [13], an L phonon is detected softening first at $\varepsilon^* = 14.736\%$ (Fig. S1), with a wave vector $\mathbf{k}^* = [111]/2$ at zone boundary and polarization vector $\mathbf{w}^* \parallel [1, 1, -1.55]$, about 7.1° deviated from the shear direction $[11\bar{2}]$ due to the shear activation volume effect [11].

We then use the same methodology applied in the main text to investigate how the softened L phonon metamorphoses into a lattice defect. An ε^*-strained Cu supercell is created with its x-axis along the shear direction $[11\bar{2}]$ and z-axis along the (111) plane normal, containing 30 (111) atomic layers in z [Fig. S2(a)]. It is perturbed according to the instability mode above with different wave amplitudes so as to get the response of the potential energy change $\Delta\Psi$ to the phonon displacement u_A. Similar to the results in Fig. 3 in the main text, $\Delta\Psi$-u_A of the supercell can also be fitted as $c_2 u_A^2 + c_4 u_A^4$ [Fig. S2(b)], which exhibits a double-well potential, in contrast to a downward parabola profile of the harmonic response. The crystal structure is transformed from the original FCC to be triclinic (TRI) when u_A gets to the well bottom. From the phonon spectra of the TRI structure along the Γ-Z path within the BZ [Fig. S2(c)], an acoustic phonon branch softens near the Γ point, indicating the TRI structure is elastically unstable for a long wave with $\mathbf{k} \parallel [001]^{\mathrm{TRI}}$. For the present supercell with a length of 15 $d^{\mathrm{TRI}}_{(001)}$ (or 30 $d^{\mathrm{FCC}}_{(111)}$), it accommodates 8 discrete k points along the Γ-Z path, and only the phonon with $\mathbf{k}$ at $[001]^{\mathrm{TRI}}/15$ is unstable, which can excite two unstable long waves, with the normalized amplitudes and the phases of their components shown in Table S2.

A perturbational plane wave according to the L phonon's instability mode is then injected into the supercell, with an initially small amplitude of 10^{-4} Å. As shown in Fig. S3(a)-(d), the perturbational wave also grows linearly first and is then trapped within a potential well, accompanied by a structural transformation from FCC to TRI. Likewise, the soft near-Γ phonon (with $\mathbf{k}$ at $[001]^{\mathrm{TRI}}/15$) of the TRI structure then excites two unstable long waves superposed upon the perturbational wave. Later, the two long waves experience amplitude growth and wave-front steepening, and the crest of the upper wave gradually approaches the valley of the lower. A Schockley partial dislocation is then nucleated [Fig. S3(e)] when the crest and valley reside on two adjacent (111) atomic layers.

As demonstrated by the example above, although the final lattice instability product, Schockley partial dislocation, is different from that in Fig. 2 in the main text, the soft phonons exhibit great similarity in their evolution featured by a two-stage soft-phonon cascade. Actually, it has been verified by our studies repeatedly, manifesting the generality of our proposed mechanism.

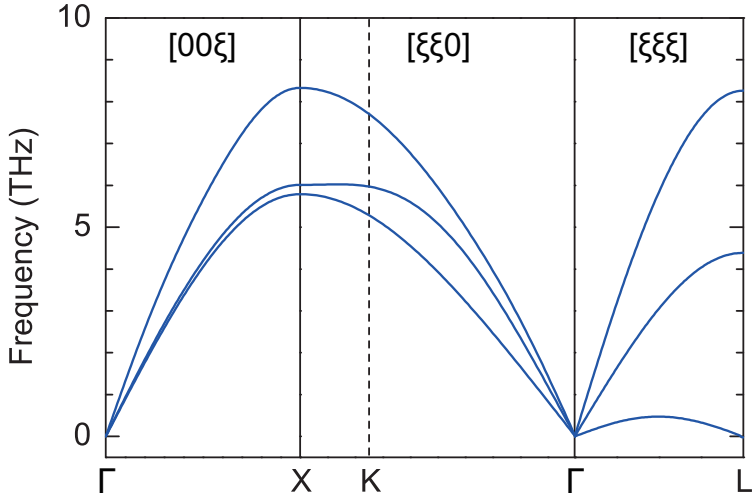

FIG. S1. Phonon spectra of Cu crystal lattice with $[11\bar{2}](111)$ shear strain of 14.736% based on the Mishin potential [13].

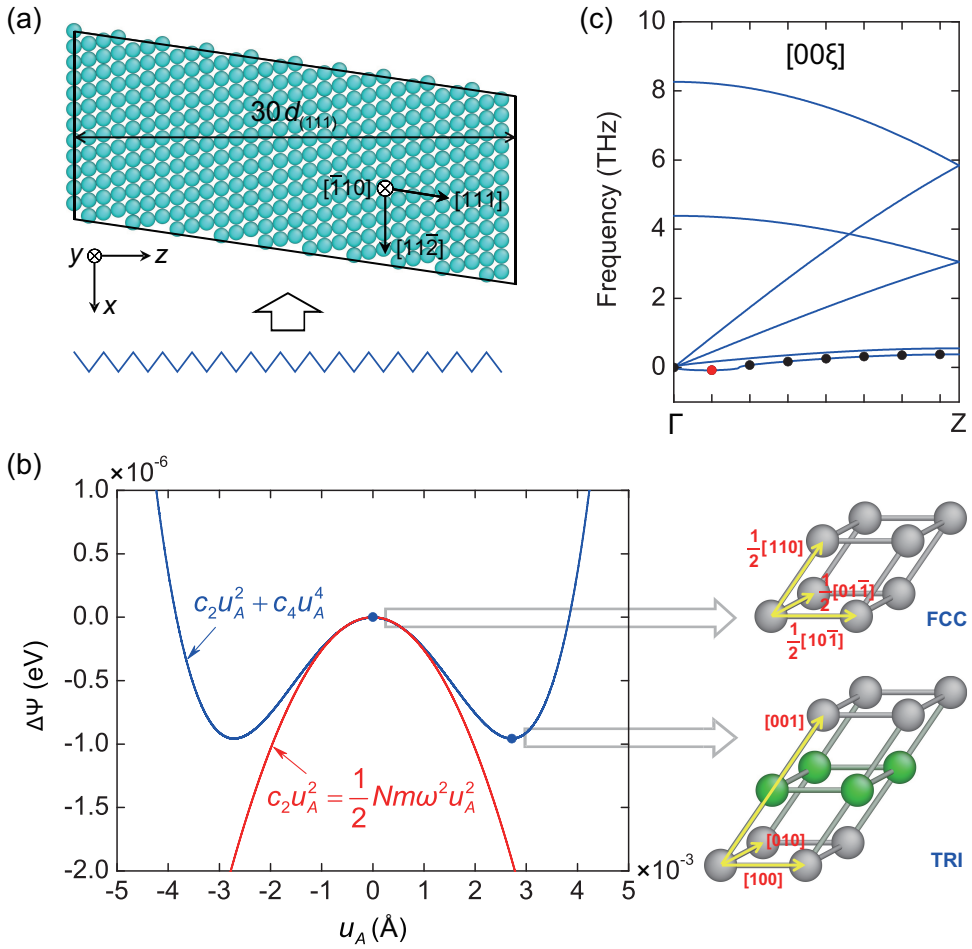

FIG. S2. Structural transformation by perturbation of an ε^*-strained Cu supercell. (a) The Cu supercell with dimensions of $l_x = 18d_{(11\bar{2})}$, $l_y = 10d_{(\bar{1}10)}$ and $l_z = 30d_{(111)}$ under PBCs, is perturbed by a plane wave according to the instability mode of the L phonon shown in Fig. S1. (b) Response of the potential energy change ($\Delta\Psi$) of the supercell to the phonon displacement (u_A) of the perturbational wave. $\Delta\Psi$ can be fitted as $c_2u_A^2 + c_4u_A^4$ (in blue), where $c_2 = -0.259$ eV/Å^2 and $c_4 = 17588.7$ eV/Å^4, compared with the harmonic-approximation response following $\Delta\Psi = c_2u_A^2 = \frac{1}{2}Nm\omega^2u_A^2$ (in red), where N is the number of atoms in the supercell, m is the atomic mass of Al, and ω is the L phonon's circular frequency ($0.148i$ THz). When u_A reaches the well bottom, structural transformation occurs from the original FCC to TRI, with their primitive cells shown on the right, and it has $d^{\mathrm{TRI}}_{(001)} = 2d^{\mathrm{FCC}}_{(111)}$. Two basis atoms in the TRI primitive cell are colored with gray and green, respectively. (c) Phonon spectra of the TRI structure along the Γ-Z path in the BZ. The supercell allows 8 discrete k points existing between [Γ, Z], of which the frequencies on the softened phonon branch are denoted as solid dots. Among those, only the k point at $[001]^{\mathrm{TRI}}/15$ has an imaginary frequency, denoted as the red dot.

TABLE S2. Normalized amplitudes (ν) and phases (φ) of the polarization components of the two unstable long waves excited by the soft phonon shown in Fig. S2(c).

Wave	Polarization components	ν	φ[a]
β_1	β_1^x	0.992	0
	β_1^y	0	-
	β_1^z	0.126	0.011π
β_2	β_2^x	0.992	0.494π
	β_2^y	0	-
	β_2^z	0.126	0.483π

[a] The values of φ given are relative to that of the β_1^x component.

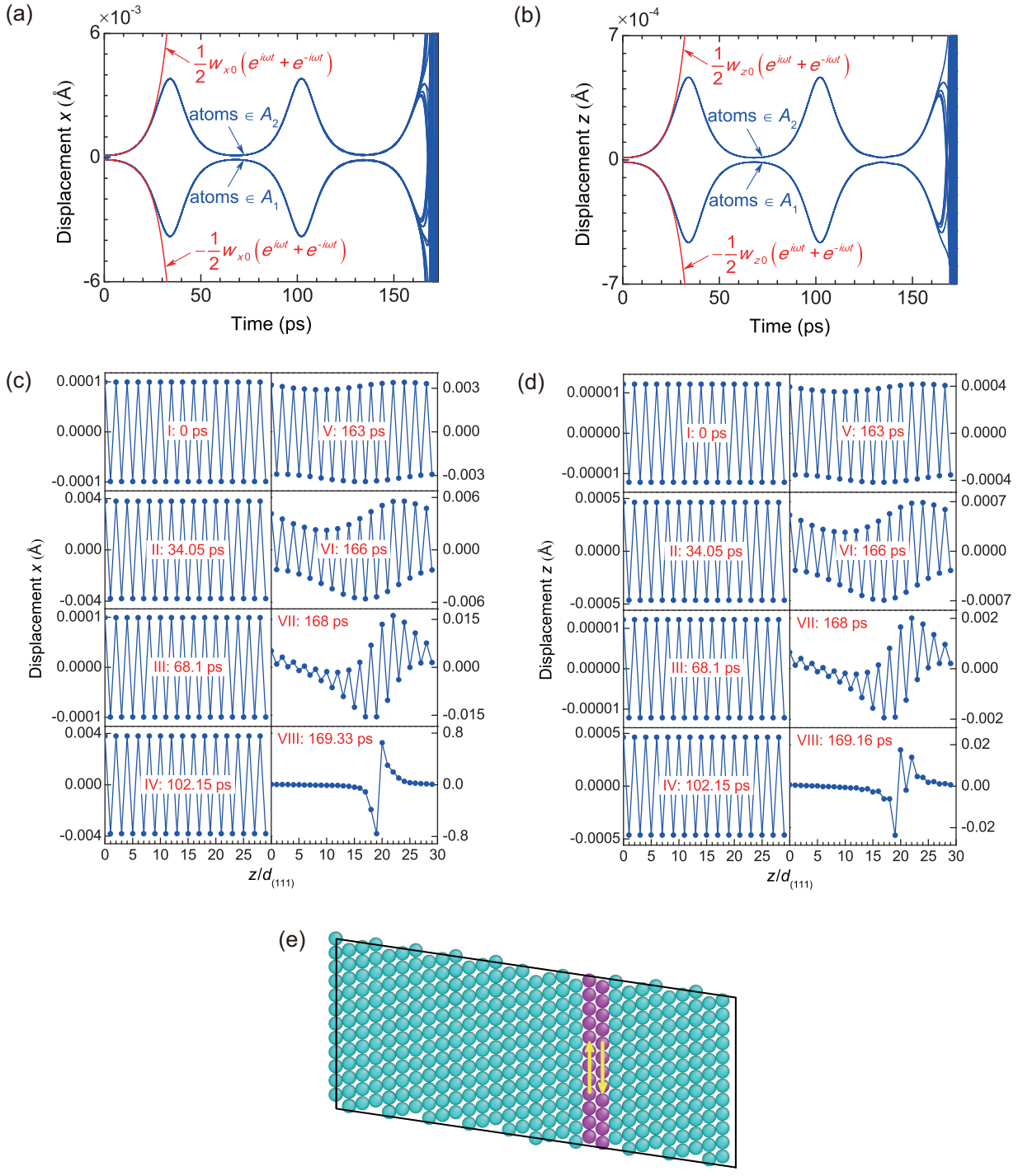

FIG. S3. Metamorphosis of the perturbed Cu supercell. (a, b) Temporal evolution of the displacements x and z of the 30 (111) atomic layers of the Cu supercell (in blue), which are initially bunched together in two groups, A_1 and A_2. They are compared with the linear growth curves (in red), in which w_{x_0} and w_{z_0} are the initial amplitude components along x and z, respectively. (c, d) Spatial evolution of the displacements x and z of the 30 (111) atomic layers, respectively. (e) Atomic configuration of the supercell at 169.33 ps, in which a Schockley partial dislocation is nucleated. The atoms are colored according to the central symmetry parameter, and the arrows denote the slip directions of the atoms on the slip plane.

VI. SUPPLEMENTARY FIGURES AND TABLES

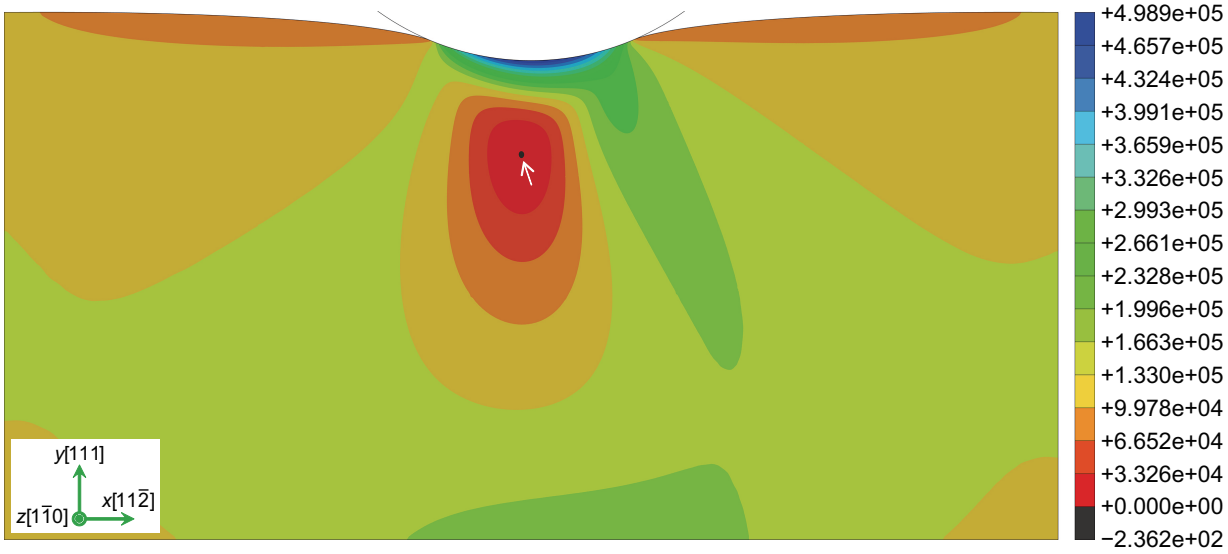

FIG. S4. Elastic instability in the Al crystal under nanoindentation predicted by the acoustic tensor formalism [14, 15]. The contour shows $|\mathbf{Q}|$ at an indentation depth of 91.5 Å by IPFEM simulation, where $\mathbf{Q}$ is the acoustic tensor, defined as $\mathbf{Q} \equiv \mathbf{n} \cdot \mathbf{L} \cdot \mathbf{n}$, in which $\mathbf{L}$ is given by $L_{ijkl} = C_{ijkl} + \sigma_{il}\delta_{jl}$, and $\mathbf{n}$ is the normal vector of a crystal plane. According to the acoustic tensor criterion, elastic instability occurs when $|\mathbf{Q}|$ vanishes for a given $\mathbf{n}$, with the associated eigenvector $\mathbf{g}$ as the slip direction. In the present simulation, the global minimum $|\mathbf{Q}|$ become non-positive first with $\mathbf{n}^0 \parallel [1\bar{1}0]$ and $\mathbf{g}^0$ approximately parallel to $[11\bar{1}]$ ($\mathbf{n}^0$ and $\mathbf{g}^0$ are the vectors scaled in the undeformed crystal), positioned at 269.2 Å beneath the top surface and 17.6 Å away from the central y axis, which is indicated by the arrow.

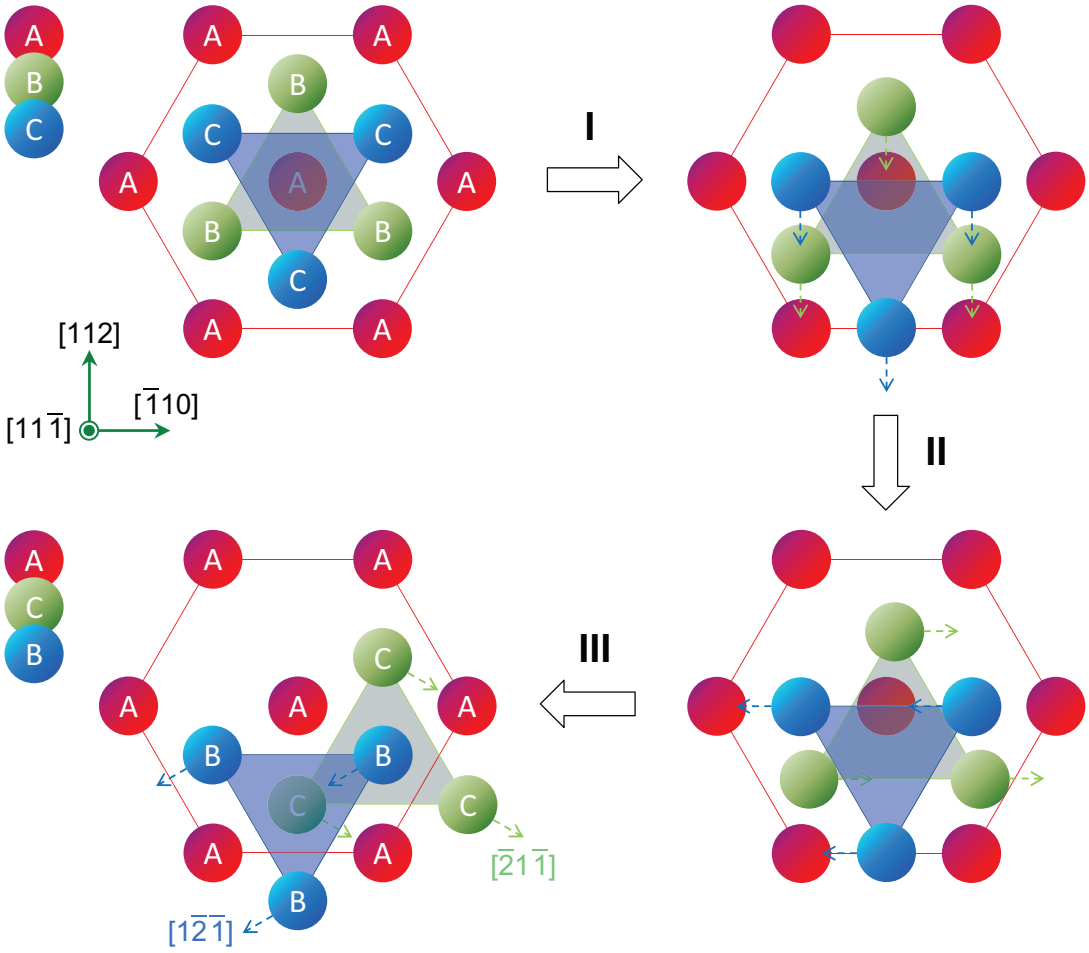

FIG. S5. Schematic of the stacking order reversing due to nucleation of a deformation twin with two different slip vectors. This process involves the following stages: (i) the lattice undergoes homogenous deformation by nanoindentation, yielding significant shear strain along the conventional anti-twinning direction of $[\bar{1}\bar{1}\bar{2}]$ on $(11\bar{1})$ plane; (ii) phase transformation from FCC to TRI occurs induced by phonon instability with $\mathbf{k}^* = [11\bar{1}]/2$ and $\mathbf{w}^* \parallel [\bar{1}10]$, with the excited lattice wave arrested by a double-well potential; (iii) a deformation twin nucleates with two different slip vectors of $\frac{1}{6}[1\bar{2}\bar{1}]$ and $\frac{1}{6}[\bar{2}1\bar{1}]$ on adjacent $(11\bar{1})$ planes, with the stacking order reversed from '$\cdots ABC \cdots$' to '$\cdots ACB \cdots$'. They are produced by $\pm\frac{1}{4}[1\bar{1}0] + \frac{1}{12}[\bar{1}\bar{1}\bar{2}] = \frac{1}{6}[1\bar{2}\bar{1}]$ and $\frac{1}{6}[\bar{2}1\bar{1}]$, respectively, arising from displacement shuffling along $[\bar{1}10]$ plus shear along $[\bar{1}\bar{1}\bar{2}]$ due to elastic instability of the TRI structure. The arrows denote the slip vectors of the upper $(11\bar{1})$ plane relative to the lower.

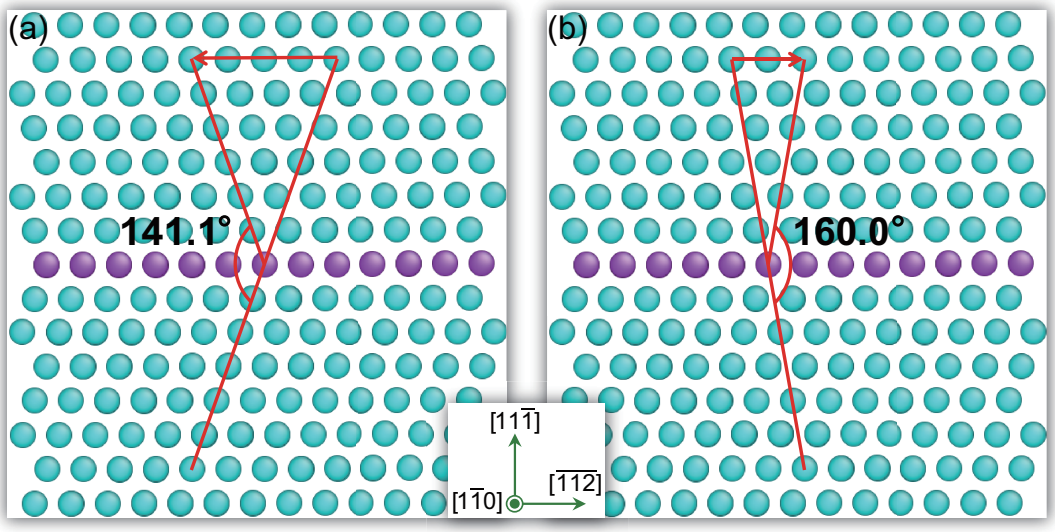

FIG. S6. Kink angles viewed from $[1\bar{1}0]$ following the (a) conventional and (b) the new homogeneous twinning mechanisms in FCC crystals. (b) has only 50% of the macroscopic strain of (a).

TABLE S3. Normalized amplitudes (ν) and phases (φ) of the polarization components of the two unstable long waves excited by the soft phonon shown in Fig. 4(a) in the main text.

Wave	Polarization components	ν	φ^{a}
β_1	β_1^x	0.763	0
	β_1^y	0.635	$-\pi/2$
	β_1^z	0.124	$\pi/2$
β_2	β_2^x	0.763	π
	β_2^y	0.635	$-\pi/2$
	β_2^z	0.124	$\pi/2$

[a] The values of φ given are relative to that of the β_1^x component.

REFERENCES

[1] R.E. Miller and D. Rodney, "On the nonlocal nature of dislocation nucleation during nanoindentation," J. Mech. Phys. Solids **56**, 1203–1223 (2008).

[2] E.B. Tadmor, M. Ortiz, and R. Phillips, "Quasicontinuum analysis of defects in solids," Philos. Mag. A **73**, 1529–1563 (1996).

[3] J. Li, K.J. Van Vliet, T. Zhu, S. Yip, and S. Suresh, "Atomistic mechanisms governing elastic limit and incipient plasticity in crystals," Nature **418**, 307–310 (2002).

[4] X.H. Liu, J.F. Gu, Y. Shen, J. Li, and C.F. Chen, "Lattice dynamical finite-element method," Acta Mater. **58**, 510–523 (2010).

[5] F. Liu, P.M. Ming, and J. Li, "*Ab initio* calculation of ideal strength and phonon instability of graphene under tension," Phys. Rev. B **76**, 064120 (2007).

[6] M.J.D. Powell, *TOLMIN: A fortran package for linearly constrained optimization calculations*, DAMTP Report NA2 (University of Cambridge, 1989).

[7] M. Born and K. Huang, *Dynamical Theory of Crystal Lattices* (Clarendon Press, Oxford, 1956).

[8] J.L. Ericksen, "The Cauchy and Born hypotheses for crystals," in *Phase Transformations and Material Instabilities in Solids*, edited by M.E. Gurtin (Academic Press, New York, 1984) pp. 61–78.

[9] M.S. Daw and M.I. Baskes, "Embedded-atom method: Derivation and application to impurities, surfaces, and other defects in metals," Phys. Rev. B **29**, 6443–6453 (1984).

[10] E.B. Tadmor, G.S. Smith, N. Bernstein, and E. Kaxiras, "Mixed finite element and atomistic formulation for complex crystals," Phys. Rev. B **59**, 235–245 (1999).

[11] J. Li, A.H.W. Ngan, and P. Gumbsch, "Atomistic modeling of mechanical behavior," Acta Mater. **51**, 5711–5742 (2003).

[12] H. Wang and M. Li, "Nonlinear theoretical formulation of elastic stability criterion of crystal solids," Phys. Rev. B **85**, 104103 (2012).

[13] Y. Mishin, M.J. Mehl, D.A. Papaconstantopoulos, A.F. Voter, and J.D. Kress, "Structural stability and lattice defects in copper: *Ab initio*, tight-binding, and embedded-atom calculations," Phys. Rev. B **63**, 2241061–22410616 (2001).

[14] R. Hill, "Acceleration waves in solids," J. Mech. Phys. Solids **10**, 1–16 (1962).

[15] J.R. Rice, "The localization of plastic deformation," in *Theoretical and Applied Mechanics*, Vol. 1, edited by W.T. Koiter (North-Holland, 1976) pp. 207–220.